Designing physicochemically-ordered interphases for high-performance composites

Sumit Gupta[1*], Tanvir Sohail[2], Marti Checa[3], Mike Toomey[1], Logan Kearney[1], Rajni Chahal[1], Sargun Singh Rohewal[1], Nihal Kanbargi[1], Swarnava Ghosh[2], Liam Collins[3], David McConnell[1], Ilia Ivanov[4], Amit K. Naskar[1], and Christopher C. Bowland[1*]

[1] Carbon and Composites Group, Chemical Sciences Division, Oak Ridge National Laboratory, Oak Ridge, TN 37830, US

[2] Advanced Computing for Chemistry and Materials Group, National Center for Computational Science, Oak Ridge National Laboratory, Oak Ridge, TN 37830, US

[3] Functional Atomic Force Microscopy Group, Center for Nanophase Material Sciences, Oak Ridge National Laboratory, Oak Ridge, TN 37830, US

[4] Functional Hybrid Nanomaterials Group, Center for Nanophase Material Sciences, Oak Ridge National Laboratory, Oak Ridge, TN 37830, US

*corresponding authors, guptas@ornl.gov, bowlandcc@ornl.gov

Abstract

To enhance the mechanical properties of carbon fiber-reinforced polymer composites, we designed a physicochemical scaffold incorporating microscopically architected chemically reactive nanofibers that act as a multiscale bridge between the carbon fibers and the matrix. Thermally activated nanofibers leverage their morphologically driven mechanochemical properties to form covalent bonds with adjacent polymer molecules, creating a co-continuous network that dramatically enhances fiber-matrix load transfer. By meticulously controlling the nanofiber architecture through variable surface area, functional group availability, and polymer chain alignment effects, we manipulated the extent of covalent bonding between nanofibers and the matrix that ultimately resulted in improved carbon fiber-matrix adhesion. We validated our concept using polyacrylonitrile nanofibers and acrylonitrile butadiene styrene as the matrix in a discontinuous carbon fiber-reinforced composite system. This approach produced immobilized, chemically transferred, and ordered nanostructures at the carbon fiber-matrix interphase, as confirmed by nanomechanical studies using atomic force microscopy and low-field NMR relaxometry. The resulting composites exhibit a ~ 56% and ~ 175% improvement in tensile strength and toughness, respectively, compared to composites without nanofiber reinforcements. Comprehensive thermal, rheological, and X-ray scattering combined with high-performance computing-enabled all-atomic molecular dynamics simulations, were conducted to uncover the fundamental mechanisms driving these improvements in mechanical behavior. The foundational insights gained from this physicochemical interphase design strategy hold promise for improving the application across various composite systems. Our approach's versatility and efficacy have the potential to effectively address longstanding interphase challenges in the composite industry.

Keywords: Fiber-reinforced polymer composites, fiber-matrix interphases, nanofibers, co-continuous, tough, multiscale

Introduction

Fiber-reinforced polymer composites (FRPCs), composed of micron-sized organic or inorganic fibers infused with thermoplastic or thermoset polymers, are widely used in aerospace, automotive, and renewable energy infrastructure due to their excellent strength-to-weight ratio [1]. Despite their benefits, the fiber-matrix interphase remains the most vulnerable region due to the mismatch in mechanical properties between the fibers and the matrix. This issue is often exacerbated by the inert physicochemical properties of fibers,

which result in weak interactions and low contact area with the matrix, leading to poor interfacial strength [2]. Extensive research has been performed to enhance the fiber-matrix interphase in FRPCs to extract higher mechanical contributions from the reinforcing fiber leading to better specific strengths.

The properties of the fiber-matrix interphase have been refined through mechanisms of physical interlocking, chemical bonding, and combinations of both. Physical interactions between carbon fiber (CF) and the matrix have been modified by introducing irregularities on the fiber surfaces via oxidization using vapor, liquid, or gas phase oxidizing agents. For example, gaseous CO_2 at ~ 900°C oxidizes CF, increasing their surface area by over 50% and enhancing composite strength by 40% [3]. Electrochemical oxidation has been demonstrated as another viable alternative that increases fiber surface roughness, leading to a 60% improvement in the epoxy matrix composite's interlaminar shear strength [4]. In addition to increasing the fiber surface roughness, the physicochemical effect was leveraged by Yu *et al*. where a liquid-phase $K_2S_2O_8/AgNO_3$ system was used to add oxygen-containing groups to CFs, boosting CF-epoxy matrix interfacial shear strength (IFSS) by ~ 60% [5]. Instead of using oxidizing agents, Zhang and Li used plasma grafting polymerization of maleic anhydride to increase surface roughness and grafted anhydride groups, creating a more active, hydrophilic fiber surface, which improved epoxy matrix composite IFSS by ~ 38% [6]. While these strategies can enhance composite interfacial properties, they incur significant costs related to chemicals, equipment, and the energy required to maintain extreme processing conditions. Precise control is essential to prevent fiber damage, further increasing expenses. Additionally, since these methods are not batch processes, they face considerable limitations, especially when requiring controlled environments away from ambient atmospheric conditions.

A more commercialized method for improving composite performance is the use of a thermoset or thermoplastic polymer-based sizing applied to the fiber surfaces, forming a protective layer that improves handling and enhances fiber-matrix adhesion through physicochemical interactions. For instance, thermoset epoxy-based emulsifiers used in aqueous media as sizing agents on CFs have shown a ~75% improvement in CF-epoxy matrix IFSS [7]. On the other hand, polyurethane-based thermoplastic sizing agents have been utilized, leading to a ~ 50% increase in CF-nylon matrix interlaminar shear strength [8]. Polydopamine chemistry has also been extensively utilized for CF sizing design. Researchers converted the amphiphobic surface of CF to a hydrophilic one using a polydopamine coating, then to oleophilic with octadecylamine grafting. Such dual-functionalization resulted in a 65% average increase in tensile properties for composites with both polar epoxy and nonpolar poly(ethylene-co-octene) as the matrix [9]. Additional surface modifications demonstrated a mussel-inspired nanohybrid sizing deposited onto CF surfaces through coincubation in a dopamine and octa-ammonium polyhedral oligomeric silsesquioxane solution, achieving a 70% improvement in IFSS [10]. Further examples of using polydopamine chemistry for CF sizing are widely documented [11]. Despite their widespread applications, the use of sizing materials is often limited by the inherently lower mechanical properties of their polymeric constituents.

Enhancing polymeric sizing materials with targeted nanomaterials can significantly improve their mechanical properties. For example, functionalized cellulose nanocrystals with 3-aminopropyltriethoxysilane enhanced the interphase between CF and an epoxy matrix, resulting in an ~ 80 % increase in IFSS [12]. Amino-functionalized ZrO_2 was incorporated on the CF surface, simultaneously strengthening and toughening the CF/epoxy composite interphase, resulting in a ~ 40 % increase in IFSS and a ~ 250 % increase in fracture toughness [13]. Introducing graphene oxide sheets in the fiber sizing of CFs increased CF/epoxy composite's IFSS by over ~ 65%, with 5 *wt*. % graphene loading [14]. Chemical modification of graphene oxide nanosheets with cyanuric chloride and diethylenetriamine significantly improved their dispersion in the sizing agent, resulting in a ~ 100% increase in IFSS even at an ~ 80% lower graphene concentration [15]. Our recent work using a roll-to-roll continuous feed-through fiber dip-coating process successfully integrated various nanomaterials onto fiber surfaces, resulting in a ~ 20% increase in interlaminar shear strength [16, 17]. However, relying solely on enhanced physical interactions

between nanomaterials and the fiber-matrix system often underutilizes their potential to elevate FRPCs' performance. Without covalent tethering of the nanomaterials to the fiber, they fail to establish a sufficiently rigid load-transfer pathway, thus limiting the full realization of interfacial strength of the bulk composite.

Instead, directly growing the nanomaterials on fiber surfaces offers a more robust approach fostering a stronger connection between the nanomaterials and the fiber, enhancing the efficacy of fiber-to-matrix load transfer. Chemical vapor deposition can be utilized to grow multiwalled carbon nanotubes onto fiber surfaces, facilitated by the deposition of catalytic nickel nanoparticles onto CFs using a low-energy double-target DC sputtering system, significantly enhancing the composites' interfacial properties [18]. This method could also be utilized for growing carbon-based nanomaterials with different form factors on the CF surfaces, repairing fiber surface defects, and promoting fiber surface roughness, resulting in ~ 175% improvement in the IFSS of the composites [19]. However, the scalability of the chemical vapor deposition method remains a concern, particularly in the composite industry where large-volume production is crucial. Elevated temperature processing poses a risk of detrimental effects on CFs, potentially compromising the overall bulk mechanical properties of the composites.

Besides growing nanomaterials on fiber surfaces, *in situ* polymerization represents a robust method for achieving precise control over polymeric structures grown on fiber surfaces, thereby enhancing fiber-matrix interfacial adhesion. For example, hexachlorocyclotriphosphazene and bis(4-hydroxyphenyl) sulfone monomers were effectively crosslinked and deposited onto the CF surface. When examined via advanced microscopy, the formation of poly(cyclotriphosphazene-co-4,4-sulfonyldiphonel) microspheres were confirmed, contributing to a notable ~ 23% enhancement in CF/epoxy composites' IFSS [20]. Grafting polymers with diverse architectures onto CF surfaces, as opposed to small functional groups, can significantly increase the number of reactive sites, enhancing surface area and roughness, thereby, potentially improving the interfacial properties of composites. Functionalizing CF with hydroxyl-terminated hyperbranched polymer via one-pot condensation of isophorone diisocyanate and tris(hydroxymethyl) aminomethane significantly enhances the interfacial properties of epoxy-based composites (~ 40% improvement in interlaminar shear strength) by increasing the polar functional groups, roughness, and wettability of the fiber surface [21]. Other polymer architecture (*e.g.*, hyperbranched aromatic polyamide) can also be grafted onto CFs via solution polymerization, significantly enhancing the IFSS by ~ 65% [22] in the CF-epoxy composites. Beyond grafting polymer molecules onto CF surfaces, studies have explored sequential assembly of two or more materials forming multilayer reinforcements via layer-by-layer assembly resulting in stronger composites. For example, a nacre-like interphase is constructed on CF by alternately depositing "rigid" polydopamine and "flexible" polyether amine via layer-by-layer assembly. This multilayer approach enhances interfacial strength and toughness through synergistic covalent bonds, hydrogen bonding, π–π stacking, and the alternating rigid-flexible structure that effectively transfers stress, offers torturous paths to crack propagation, and induces viscoplastic energy dissipation [23].

Despite advances in interphase engineering, in general, current methods often rely on expensive reagents and harsh conditions, necessitating the development of simpler experimental techniques and fewer materials to facilitate the transition from laboratory-scale to mass production. While most research has focused on CF surface modification, optimizing both matrix and fiber simultaneously and creating a co-continuous interphase scaffold with intermediate mechanical properties could distribute stress more uniformly, extending crack propagation paths and enhancing mechanical properties. However, the benefits of such co-continuity by leveraging nanomaterials networks are still limited especially due to the limited length scales of the nanomaterials that can potentially be avoided by either synthesizing long-aspect ratio nanomaterials, increasing their surface areas, and facilitating covalent bonding in a more controlled fashion.

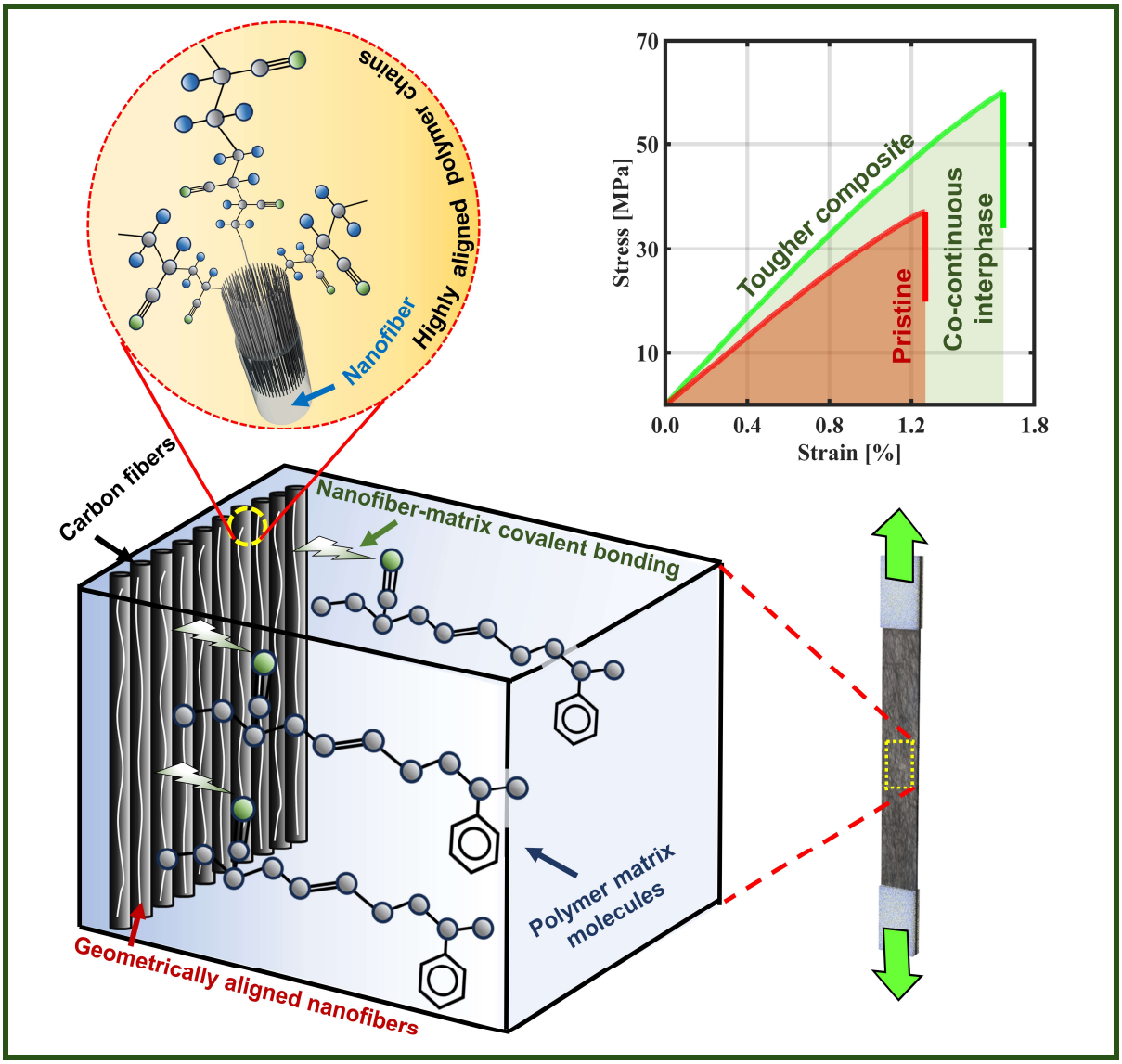

Fig. 1. Schematic illustration of co-continuous interphase in carbon fiber-reinforced composites, achieved by leveraging the physicochemical scaffolding effect of nanofibers. FRPCs often exhibit limited mechanical properties due to inadequate fiber-matrix interaction (red curve). Functional nanofibers introduced at the carbon fiber-matrix interphase form covalent bonds with the matrix while strengthening themselves via self-cyclization upon simple heat treatment. The nanofiber architecture is controlled by aligning them geometrically and orienting the polymer chains axially. This alteration also modifies their surface area, molecular chain alignment, and the number of available functional groups to bond with the matrix. By meticulously designing the nanofiber architecture and facilitating their intra- and inter-chain cyclization within themselves and with the polymer matrix, through simple heat treatment, produced a tougher composite (green curve).

With diameters ranging from 10 to 500 nm, polymeric nanofibers could be fabricated by scalable, low-cost fabrication methods, exhibiting high surface area-to-volume ratios, and distinctive size-dependent mechanical responses [24]. These properties, linked to their nanostructures, have been extensively studied through experimental and computational methods. One of the primary explanations for the size-dependent mechanical properties in polymeric nanofibers is the chain alignment effect, attributed to size-dependent microstructural changes induced during nanofiber fabrication [25]. While these properties have been well-documented [26-28], their impact on the fiber-matrix interface in bulk composites remains unexplored. Our

prior work with nanofiber-aided bridging between CF and matrix delivered a toughened composite [29]. Enhancing fiber-matrix interfaces through CF-matrix non-bonded interactions augmented by chemical interactions between nanofibers and the matrix, may be insufficient to fully exploit the co-continuity potential of nanofibers in interphase design. The pressing scientific challenge is to determine how multiscale architecture of these nanofibers can amplify both physical and chemical reinforcement effect, thereby creating a more robust CF-matrix interphase. Understanding the role of nanofiber' multiscale architecture could unlock transformative interfacial properties, advancing composite performance far beyond current limitations.

This paper investigates the efficient integration of nanofibers at the CF-matrix interfaces while controlling their physicochemical architecture, including aspect ratio, surface area, and surface functional group density, to design CF-matrix graded interphases for improved load transfer. We hypothesize that nanofibers featuring optimized physicochemical architecture with sufficient mechanical attributes, when covalently bonded with adjacent matrix molecules, can create a robust co-continuous network at the CF-matrix interphase enhancing interfacial load transfer. This study is the first to report on the effect of nanofiber intra-chain cyclization and nanofiber-matrix inter-chain chemical bonding and its control through polymer chain alignment and nanofiber surface area. We explore the dependency of nanofiber physicochemical architecture and composite interfacial properties from atomic to bulk scale. To test our hypothesis, electrospun polyacrylonitrile (PAN) nanofibers were used, as their architecture can be easily adjusted by modifying electrospinning parameters. Acrylonitrile butadiene styrene (ABS) was selected as the matrix for its compatible nitrile groups, enabling covalent bonding with PAN nanofibers upon heat treatment. The number of available functional groups on nanofibers for covalent bonding with the matrix was controlled by altering the nanofibers' surface area. This, along with nanofiber geometric and chain alignment, was utilized to enhance the reinforcing effect at the fiber-matrix interface as schematically shown in **Fig. 1**. We employed multiscale thermomechanical experiments to thoroughly characterize the reinforcing action. Additionally, all-atom molecular dynamics models of the CF-nanofiber-polymer matrix system were developed, and their interfacial mechanical properties were assessed through *in silico* mechanical testing. The results from both experimental and computational studies are summarized below.

Results and Discussions

Tuning the multiscale architecture of nanofiber scaffold

For all experimental studies, PAN nanofibers were electrospun from a 5 *wt*.% PAN solution that was prepared by dissolving the required amount of PAN powder in dimethylformamide (DMF), as detailed in the experimental procedures section. Electrospinning was employed to produce nanofibers with tunable architecture. The schematic of the electrospinning setup is presented in **Fig. S1**. Among the various techniques to modify the diameter of electrospun nanofibers and their subsequent surface area, adjusting the electrospinning voltage (V) is an effective and straightforward method for controlling the diameter of PAN nanofibers, while maintaining other electrospinning parameters constant. To verify, PAN nanofibers were deposited on aluminum foil wrapped around a collecting drum maintained at low rpm (500 rpm). V was systematically varied, and the nanofibers were collected for ~ 30 s and analyzed using scanning electron microscopy (SEM) (**Fig. 2A**). Additional SEM micrograms are provided in **Fig. S2**. A customized image processing algorithm was employed to measure the diameters of the deposited nanofibers. The resulting diameter distributions are presented in **Fig. 2B**. **Fig. 2C** summarizes that the average nanofiber diameter decreased from ~ 0.40 μm to ~ 0.18 μm when V was reduced from 20.5 kV to 6.5 kV. At high voltages, coulombic forces surpass viscoelastic forces, causing the overstretched charged jet to potentially break and reach the grounded target more quickly. This rapid travel time allows less solvent evaporation, resulting in larger and more irregular fiber diameters [30].

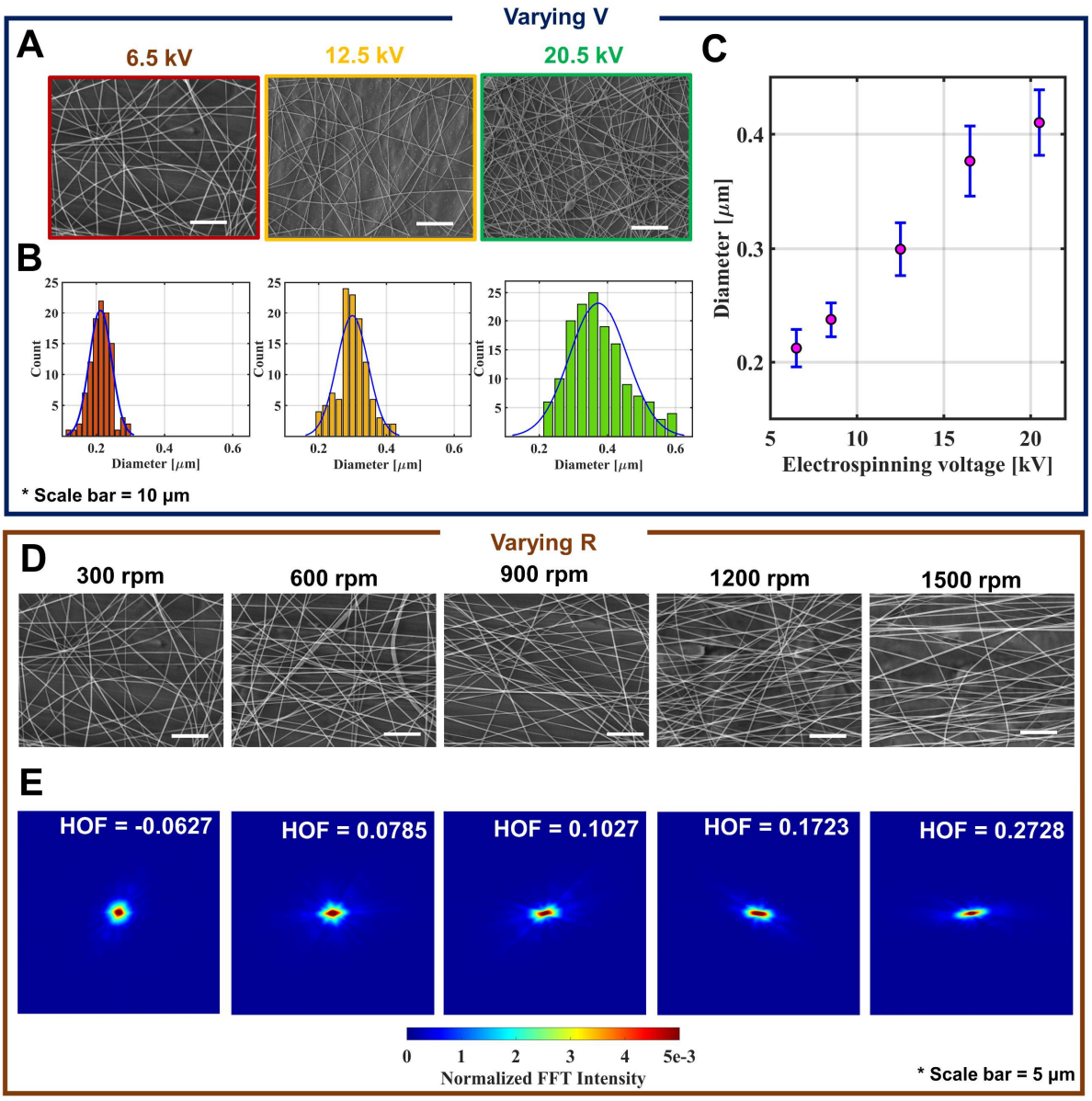

Fig. 2. Morphological characterization of electrospun PAN nanofibers. (A) SEM images of nanofibers produced at varying electrospinning voltages (6.5 kV, 12.5 kV, and 20.5 kV) and **(B)** their diameter distributions are shown. **(C)** The plot highlights the trend in nanofiber diameter as a function of electrospinning voltage. Error bars indicate the standard deviation across measurements within the same image. **(D)** SEM images of PAN nanofibers obtained at different collecting drum rotational speeds (300 rpm to 1,500 rpm) while keeping the V at 6.5 kV and **(E)** shows the corresponding FFT intensity plots and calculated HOF values.

Given that the electrospinning volume was maintained at 0.75 mL/h, and the nanofibers became finer as V decreased, it follows that the total surface area of the nanofibers increased. Consequently, the maximum surface area was achieved at the minimum V. Maximizing the surface area ensures greater availability of functional groups on the nanofiber surfaces, facilitating enhanced covalent bonding with the adjacent matrix molecules. However, low voltage may not generate fibers with sufficient volume, indicating a trade-off between achieving the smallest nanofiber diameter and production volume. In our study, we determined that 6.5 kV is the optimal voltage, producing fibers with minimal diameter and maximal surface area while maintaining an adequate volume. Smaller diameter is noteworthy for potentially enhancing polymer chain

alignment within PAN nanofibers, which could be advantageous for designing stronger multiscale scaffolds at fiber-matrix interfaces, thereby improving mechanical performance in bulk composites. This capability plays a crucial role in our study's approach to controlling the physicochemical architecture of scaffold, as thoroughly characterized later in this investigation.

Reducing the diameter of PAN nanofibers can enhance mechanical properties such as tensile strength, elastic modulus, and toughness. However, there exists an optimal diameter threshold beyond which further reduction may not yield additional benefits and could even be detrimental. Studies have indicated that nanofibers with diameters around 500 nm exhibit significant improvements in mechanical characteristics [31]. Beyond this point, further decreasing the diameter can lead to challenges such as increased surface energy and potential structural instability, which may compromise the mechanical integrity of the fibers. A similar trend was reported by Naraghi *et al*., who observed that the mechanical properties of electrospun PAN nanofibers improved as the nanofiber diameter decreased, reaching an optimum around ~ 300 nm [32]. Beyond this threshold, further reductions in diameter resulted in a decline in yield stress and Young's modulus. They attributed this to the production method of the larger-diameter nanofibers, which involved reducing the spinning distance (i.e., the distance between the spinning needle and the collector). This shorter travel distance likely limited solvent evaporation, leaving a higher solvent content in the nanofibers. As a result, the PAN chains in these nanofibers exhibited reduced molecular alignment, adversely affecting their mechanical performance. In summary, while smaller diameters can be advantageous, there is a critical limit, and optimizing nanofiber diameter is essential to balance mechanical performance and structural stability. In our study, we have demonstrated that smaller-diameter PAN nanofibers significantly enhance the mechanical properties of PAN-ABS composites, with composites containing 0.21 μm diameter nanofibers outperforming those with larger diameters. While we aimed to fabricate even smaller-diameter nanofibers using our current electrospinning setup, the process was unsuccessful. Specifically, reducing the voltage below 6.5 kV, a critical threshold for forming a stable Taylor cone, resulted in incomplete PAN nanofiber deposition. We hypothesize that there exists an optimal nanofiber diameter, below which further reductions will not yield additional mechanical performance improvements due to diminishing structural or interfacial benefits. However, generating PAN nanofibers smaller than 0.21 μm to test this hypothesis would require modifications to electrospinning conditions, such as dope formulation or air gap length, that would introduce variables into the equation creating complications in accurately comparing different nanofiber dimeters.

To maximize the mechanical performance of composites, we collected oriented nanofibers in the direction of the drum's rotation. We ensured that, within the composite laminates, the applied load was always aligned with the axial direction of these oriented nanofibers, optimizing the mechanical properties of the resulting composites. We controlled

the rpm of the collecting drum (*r*) and the collected specimens were examined under SEM, with representative micrographs shown in **Fig. 2D**. We found that as *r* increased, the enhanced mechanical drawing force improved fiber alignment along the horizontal direction of the SEM micrograph, whereas at lower speeds, the collecting drum lacked sufficient force to counteract bending instability, resulting in the deposition of randomly oriented nanofibers. To further quantify the results, we calculated the Fast Fourier Transform (FFT) intensities of the collected SEM images (**Fig. 2E)**. Since more fibers horizontally aligned at higher *r*, the central circle in the FFT diagram became elliptical, with its major axis oriented in the direction of predominant nanofiber alignment. Herman's Orientation Factor (HOF) was derived from these FFT intensity plots which is a mathematical measure of line structure alignment relative to a reference direction [33]. HOF ranges from -0.5 to 1, where -0.5 indicates perfect perpendicular alignment, 1 represents perfect horizontal alignment, and 0 signifies random orientation. More details about HOF can be found elsewhere [34]. In our study, the HOF value at 300 rpm specimen was ~ -0.06, indicating a nearly random orientation of the nanofibers within the micrograph. As *r* increased to 1,500 rpm, the HOF value rose to 0.27, signifying a maximal alignment of the nanofibers in the horizontal direction. Overall, the

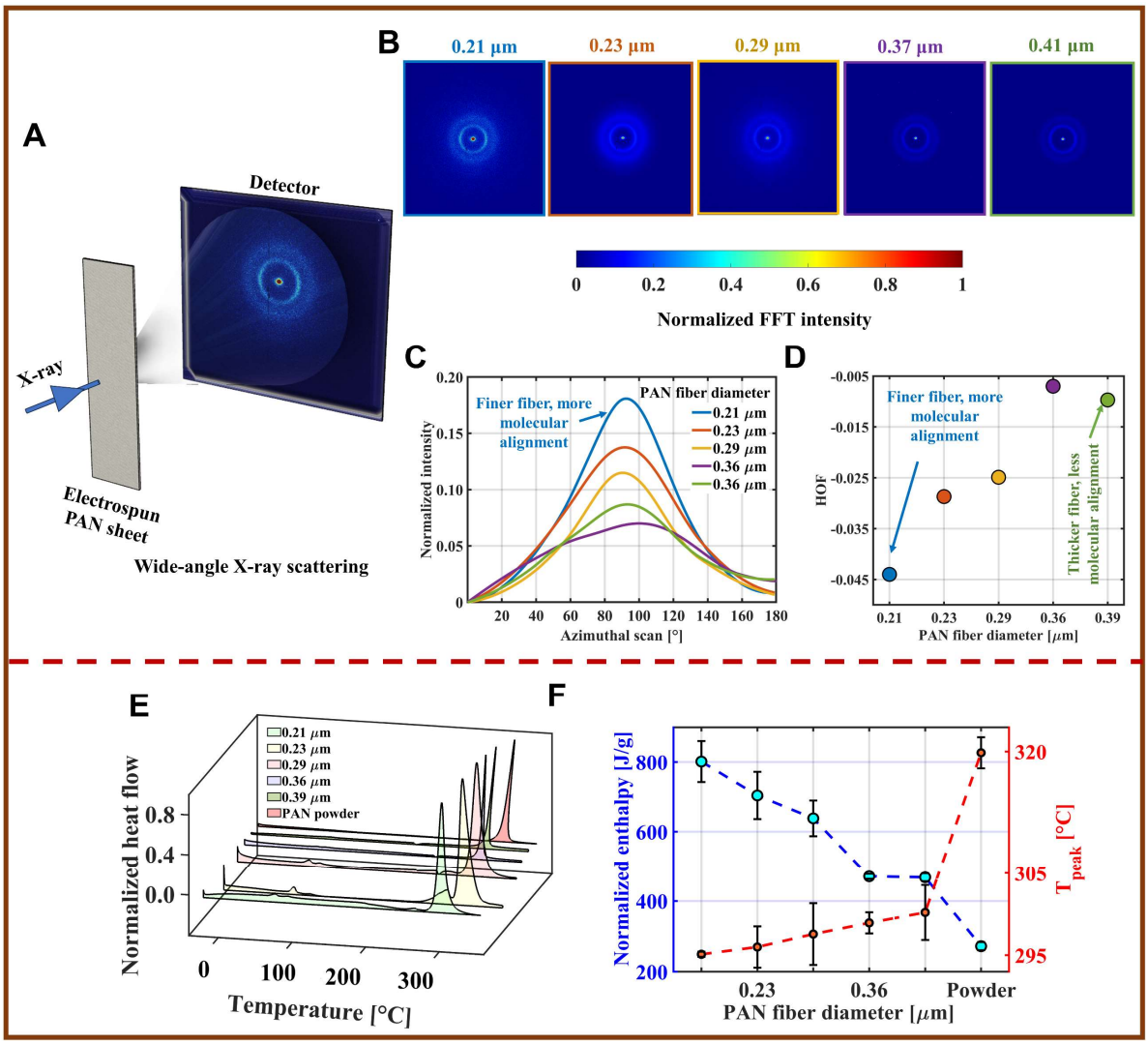

Fig. 3. Characterization of PAN chain alignment in PAN nanofibers using WAXS and DSC. (A) Schematic of the WAXS setup used for analyzing PAN chain alignment within individual PAN nanofiber sheets. **(B)** FFT intensity plots from WAXS data. **(C)** Orientation distribution of PAN chains within nanofibers of varying diameters. **(D)** HOFs show the degree of PAN chain alignment across different diameters. **(E)** DSC thermograms showing temperature vs. heat flow for nanofibers with varying diameters. **(F)** Variation in enthalpy and peak temperature for different diameter PAN nanofibers with error bars indicating standard deviation in measurements in five specimens.

results presented in **Fig. 2** demonstrate that electrospinning is an effective method for producing nanofiber scaffolds with diverse architectures, which can be readily incorporated at the CF-matrix interfaces to improve the interfacial strength of composites**.**

In addition to utilizing the microscopic architecture of nanofibers to enhance composite strength, the orientation of molecular PAN chains can be controlled by manipulating V thus maximizing their axial mechanical properties [35]. Such ability to control the nanofiber architecture across multiple length scales can be strategically harnessed to enhance the design of high-performance composites, as previously mentioned. To investigate the molecular alignment of PAN chains within individual nanofibers, PAN nanofiber sheets were prepared and investigated via WAXS (**Fig. 3A**). WAXS patterns were collected from the sheets of nanofibers electrospun at different V with r = 1,500 rpm. High r was maintained to minimize geometric broadening of the aligned PAN nanofibers in WAXS. The diffraction patterns shown in **Fig. S3**,

revealed two equatorial peaks located at scattering vectors (Q $Å^{-1}$) of approximately 1.2 and 2, attributed to the hexagonal packing of 100 and 110 crystal planes, respectively. The 110 scattering feature indicates

the onset of an oriented microstructure bearing peak scattering intensity perpendicular to the primary fiber axis. Analysis of the azimuthal profiles were performed to determine the degree of molecular orientation within the fibers as the spinning parameters were varied (**Fig. 3C**). The highest intensity at a 90° azimuthal angle was observed for $PAN_{0.21\mu m}$ nanofibers, which decreased with increasing fiber diameter (**Fig. 3C**). The subscript with PAN indicates their average diameter. The HOF of $PAN_{0.21\mu m}$ nanofibers is ~ -0.045, approaching zero (~ -0.005) for $PAN_{0.39\mu m}$. This indicates that $PAN_{0.21\mu m}$ nanofibers, exhibit better molecular alignment than $PAN_{0.39\mu m}$. The calculated HOFs for PAN nanofibers spun at various *V*s are presented in **Fig. 3D**. During electrospinning, lower *V* leads to better polymer chain alignment due to reduced jet instability, slower jet stretching, and more controlled deposition. Additionally, slower stretching allows more time for polymer chains to align, and reduced charge density on the polymer solution enables closer chain packing and better alignment [36, 37].

Fig. 3E presents the DSC heating scans of PAN nanofiber sheets electrospun at varying *V*. All PAN specimens exhibited a pronounced exothermic peak between 295°C and 320°C, attributed to the cyclization of PAN molecules, resulting in the formation of conjugated carbon-nitrogen sequences [38]. The enthalpy of exothermic heat for this reaction is significantly greater in electrospun fibers compared to $PAN_{powders}$, with the highest values observed in the most molecularly aligned nanofibers (*i.e.*, $PAN_{0.21\ \mu m}$) as summarized in **Fig. 3F**. The observed increase in enthalpy in the DSC study could be partly due to residual DMF retained within the electrospun PAN nanofibers. However, the primary factor likely remains the enhanced cyclization efficiency of the smaller-diameter nanofibers. Simultaneously, the peak temperature decreases in electrospun samples, reaching the lowest value in $PAN_{0.21\ \mu m}$. Specifically, the peak temperatures are ~ 319°C for PAN_{powder}, ~ 300°C for $PAN_{0.39\ \mu m}$, and ~ 295°C for $PAN_{0.21\ \mu m}$. The enhanced exothermic heat and corresponding reduction in cyclization temperature from less-aligned to most-aligned PAN nanofibers can be attributed to the increased macromolecular orientation in the specimens, promoting a more efficient intra- and inter-chain cyclization reaction. Similar findings were reported following hot-stretching of PAN electrospun fibers to boost polymer crystallinity [39]. Overall, **Figs. 3E-3F** demonstrates that lower *V* produces PAN fibers with smaller diameters, higher surface areas, and better chain alignment. The increased surface area of the nanofibers, combined with the higher density of exposed nitrile groups, may promote stronger chemical bonding with matrix molecules during heat treatment. Additionally, improved chain alignment in the nanofibers can result in more robust scaffolds for stronger interphase design.

Exploring the architectural influence of PAN nanofibers on PAN-ABS covalent interactions

Our next objective is to demonstrate that these better-aligned PAN chains, with higher surface area, form more covalent bonds with the ABS matrix. We prepared PAN-ABS composites by incorporating electrospun PAN nanofibers (spun at various *V*) in ABS by means of melt-mixing at an ultra-low concentration of 0.02 *wt*.%. Such concentration was maintained to match the deposition weight fraction on CF from only ~ 30 s of electrospinning that was performed to fabricate the composites later in this study. To estimate the weight percentage of nanofibers within the composites, we employed an image processing-based method. This approach is thoroughly detailed in the current study, with additional insights available in our previous work [29]. This study revealed that just ~ 30 seconds of electrospinning incorporates approximately 0.02 *wt*.% of PAN nanofibers into the entire composite. The resulting mixture was then hot-pressed at ~ 250˚C for ~ 30 mins into 1-mm-thick sheets and used in PAN-ABS covalent bonding validation via solubility, rheology, and dynamic scanning calorimetry (DSC) experiments. More details about the sample preparation can be found in the experimental procedure section. Although our DSC analysis shows that PAN nanofibers undergo cyclization around 300˚C, heating above 250˚C initiates ABS thermal degradation, severely compromising the mechanical strength of PAN-ABS composites. Szepcsik

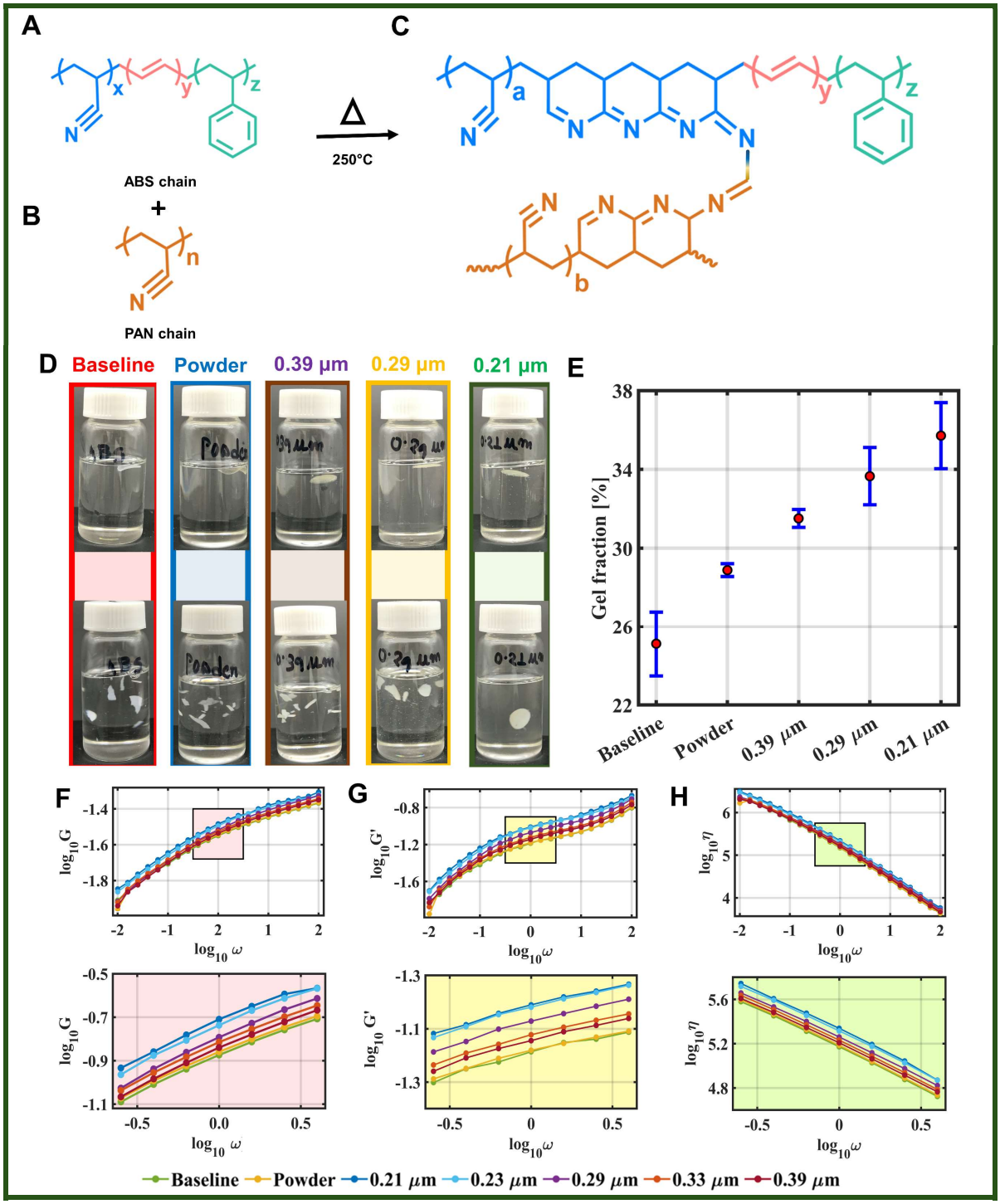

Fig. 4. The degree of crosslinking between PAN nanofibers with different diameter and ABS heat-treated at 250°C is analyzed. **(A)** and **(B)** shows the chemical structures of the PAN and ABS molecules, respectively, while **(C)** is the probable covalently bonded PAN-ABS structure. **(D)** shows the solubility test specimens before and after the 24 h solubility study. **(E)** presents the gel fraction of these PAN-ABS specimens with different PAN nanofiber diameters. Error bar indicates the standard deviation from five sample sets. **(F)**, **(G)**, and **(H)** the variation in G, G', and η of PAN-ABS specimens with PAN nanofibers of different diameters. The corresponding insets provide a zoomed-in view of the three material properties highlighted in the colored boxes in **(F)**, **(G)**, and **(H)**. The units of G, G' are both in MPa while complex viscosity is Pa. S and the ω is in rad/s.

and Pukánszky reveal that PAN nanofibers can achieve significant intra- and inter-chain crosslinking at approximately 250˚C - right within the threshold that preserves ABS integrity [40]. This insight underscores the potential for optimizing crosslinking without sacrificing composite performance. Since PAN and ABS have similar nitrile groups (**Figs. 4A** and **4B**), we hypothesize that similar interchain crosslinking could occur between PAN and ABS chains in parallel to intra-chain crosslinking within PAN, resulting in a ladder-like covalently-bonded structure required for co-continuous interphase formation within FRPCs. The extent of such crosslinking will depend on the availability of nitrile groups on the surface of PAN nanofiber. **Fig. 4C** illustrates the anticipated chemical reaction and the resulting PAN-ABS bonded structure.

Figs. 4D showcase the results of the solubility tests conducted on the PAN-ABS composites. Neat ABS and $PAN_{0.39\mu m}$-ABS, as well as $PAN_{0.29\mu m}$-ABS specimens, disintegrated into smaller fragments, whereas the $PAN_{0.21\mu m}$-ABS specimen, although swollen, remained intact. This visual inspection clearly demonstrates that the PAN-ABS specimen with smaller diameter PAN nanofibers exhibits superior integrity compared to the other specimens, indicating a higher degree of PAN-ABS covalent bonding. For better quantification, we calculated the gel fraction of the PAN-ABS composites and summarized in **Fig. 4E**. We found that the gel fraction of the PAN-ABS composites increases in a monotonic fashion with the decreasing PAN nanofiber diameter. For example, gel fraction of neat ABS was ~ 25% increased to ~ 29% in PAN_{powder}-ABS, then to ~ 31% in the case of $PAN_{0.39\mu m}$-ABS and then goes to ~ 36%, which is almost 35% higher than neat ABS. The smaller diameter PAN nanofibers provide a higher surface area, exposing more nitrile groups that can form covalent bonds with adjacent ABS molecules during heat treatment resulting in a higher gel fraction compared to composites containing larger diameter PAN nanofibers. This observation validates our hypothesis, highlighting the importance of nanofiber diameter and surface area in the formation of covalently interconnected PAN-ABS network.

Given that PAN-ABS covalent bonding alters the viscoelastic properties of the composites, dynamic oscillation rheology provides a straightforward validation of PAN-ABS covalent bonding. The storage modulus (G) and loss modulus (G'), measured as functions of angular frequency (ω), provide insights into the elastic and viscous behaviors, respectively. A higher crosslink density typically results in an increased G', reflecting a more covalently bonded network [41]. **Figs. 4F** and **4G** illustrate the variation in G and G', respectively, for different specimens, showing an increase in both G and G' as the nanofiber diameter decreases from 0.39 μm to 0.21 μm. For instance, G for neat ABS at ~ 2.5 rad/s is 0.17 MPa, which increases to 0.18 MPa for $PAN_{0.39\mu m}$-ABS composites and further to 0.25 MPa in $PAN_{0.21\mu m}$-ABS composites. In the case of G', it changes from 0.07 MPa to 0.074 MPa and then to 0.11 MPa for $PAN_{0.21\mu m}$-ABS composites. A similar trend is observed in complex viscosity (η) (**Fig. 4H** and inset), which rises from 6.3×10^4 Pa·s for neat ABS to 1.09×10^5 Pa·s, in case of $PAN_{0.21\mu m}$-ABS composites. These results also indicate that PAN nanofibers with smaller diameters and higher surface areas possess more reactive nitrile groups, leading to increased covalent bonding with adjacent ABS molecules' nitrile groups upon heat treatment. This enhanced viscoelasticity validates our hypothesis.

The extent of PAN-ABS covalent bonding with respect to the PAN nanofiber diameter was investigated by characterizing their glass transition temperature (T_g) through DSC. All DSC plots for the tested specimens are provided in **Fig. S4**. The estimated T_g values are summarized in **Fig. S5**. It is evident that increasing the PAN nanofiber surface area (*i.e.*, decreasing nanofiber diameter) results in an increase in T_g, indicating a higher presence of immobilized fractions and fewer rubbery, flowable components within the composites. For example, neat ABS exhibits a T_g of ~ 94°C, which increases to 97°C in PAN_{powder}-ABS composites. This value further rises by ~1°C in $PAN_{0.39\mu m}$-ABS composites and reaches 98°C in $PAN_{0.21\mu m}$-ABS composites, likely due to increased surface area-driven crosslinking of PAN nanofibers with the adjacent ABS matrix. Overall, our observation about T_g with respect to PAN nanofiber diameter/ surface area is consistent with our previous observation during solubility and rheology study. The influence of PAN nanofiber diameter on PAN-ABS covalent bonding was also evaluated by analyzing their thermal behavior

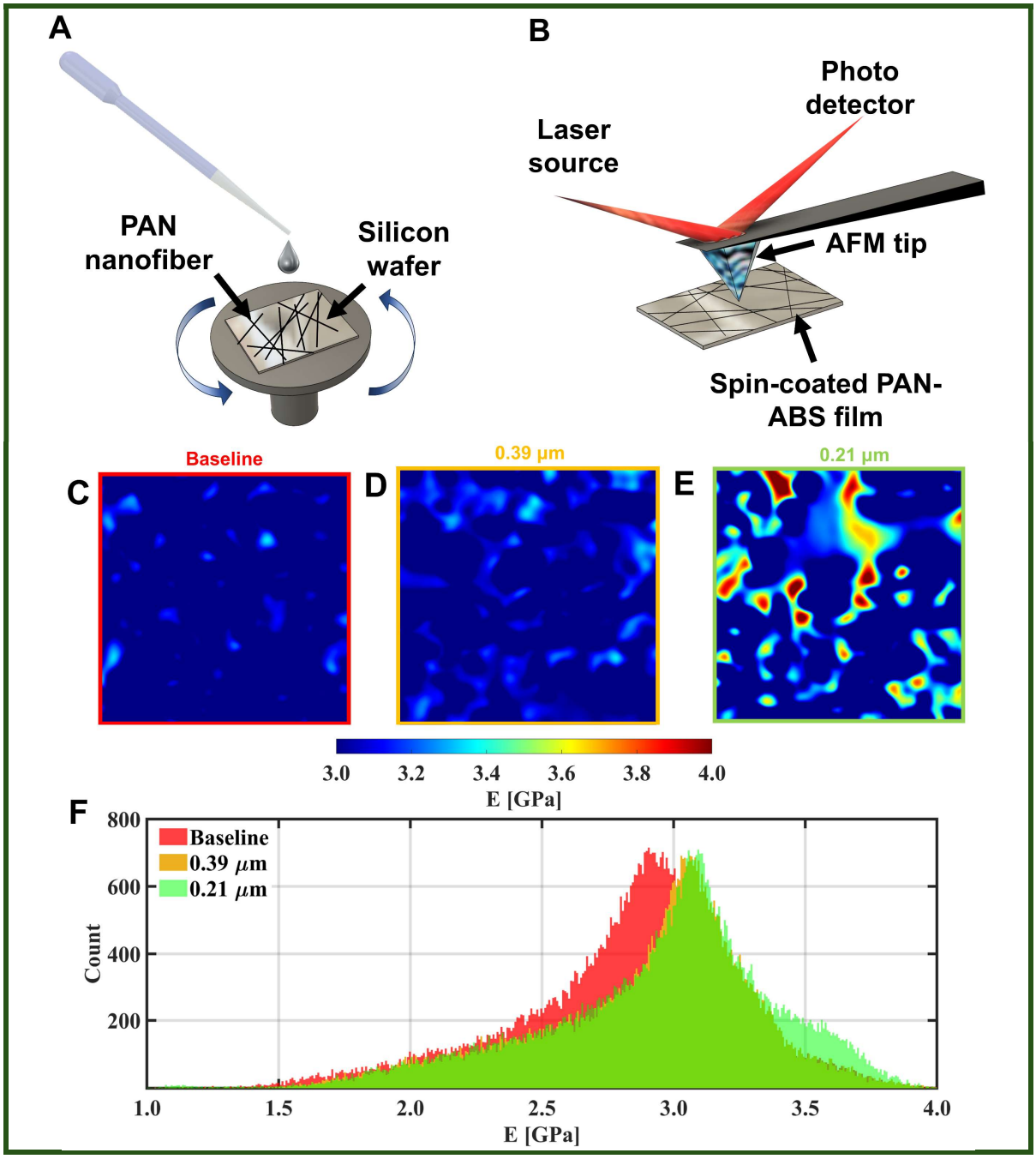

Fig. 5. AFM-based nanoindentation was conducted to precisely characterize the mechanical properties of PAN-ABS composites with different diameter PAN nanofibers. (A) PAN-ABS composite films were prepared via spin-coating and **(B)** scanned using tapping mode AFM. **(C)**, **(D)**, and **(E)** are the filtered *E* maps of neat ABS, $PAN_{0.39\mu m}$-ABS, and $PAN_{0.21\mu m}$-ABS, obtained from AFM analysis. **(F)** Histogram represents the distribution of *Es* obtained from image analysis of three separate PAN-ABS specimens.

using TGA. TGA results for selected PAN-ABS composites are shown in **Fig. S6A**. The inset highlights the thermal degradation trends of PAN-ABS composites within the 310–350°C range, revealing that $PAN_{0.21\mu m}$-ABS composites exhibit the lowest degradation rate, which increases within increasing PAN nanofiber diameter. Furthermore, neat ABS begins thermal degradation above 250°C (**Fig. S6B**), with its peak degradation temperature occurring around 420°C. Therefore, processing PAN-ABS composites at 250°C

does not significantly degrade the ABS, confirming that the processing conditions used are well within the thermal stability limits of the matrix.

After confirming that PAN-ABS covalent bonding is influenced by the surface area of PAN nanofibers, we aimed to leverage this for improved mechanical properties in PAN-ABS composites. Our goal was to study the spatial stiffness distribution of PAN-ABS composites with varying PAN nanofiber diameters. The hypothesis is that higher surface area PAN nanofibers would form more covalent bonds with the ABS matrix, making smaller diameter PAN nanofiber composites stiffer. We prepared PAN-ABS films by depositing PAN nanofibers on a silicon wafer, followed by spin-coating with an ABS-acetone emulsion (**Fig. 5A**). Details on the sample preparation process are provided in the experimental procedure section. A nanoindentation test was performed using atomic force microscopy (AFM) in AM-FM mode [42] for surface nanomechanical characterization of PAN-ABS composites. In short, by fitting the local indentation data to the Hertz model, the method yields spatially resolved stiffness maps. Leveraging the known mechanical properties of the AFM tip, the local Young's modulus (E) was quantified at each point on the specimen. The raw AFM-derived E maps are shown in **Fig. S7**. These maps were processed with a Gaussian image filter and are displayed in **Figs. 5C-5E**. In **Fig. 5C**, the E map for neat ABS shows lower average stiffness. The $PAN_{0.39\mu m}$-ABS composite (**Fig. 5D**) exhibits stiffer regions indicated by greenish-blue spots. The $PAN_{0.21\mu m}$-ABS composite (**Fig. 5E**) shows a significant increase in higher stiffness regions marked in red. Histograms of these E maps (**Fig. 5F**) further quantify that neat ABS has a peak stiffness of ~ 2.9±0.5 GPa, while $PAN_{0.39\mu m}$-ABS and $PAN_{0.21\mu m}$-ABS composite reach ~ 3.1±0.5 GPa and ~ 3.1±0.6 GPa, respectively, obtained by fitting a Lorentzian distribution to the histograms of the E maps. $PAN_{0.21\mu m}$-ABS has more pixels showing higher E values (>3.2 GPa) than the other two specimens, as indicated by a histogram hump, due to increased fiber surface area for PAN-ABS covalent bonding. It is crucial to acknowledge that AFM, being primarily surface-sensitive, probes only the top few nanometers of the material. While this may limit its ability to capture the full bulk mechanical response, the technique still reveals meaningful insights. Notably, global stiffening effects are subtly transduced into surface mechanical changes, as evidenced by the distinct color contrasts in the E maps. However, the results are influenced by factors such as the scanned region, local topography, and sample thickness, which could raise concerns about statistical significance. Moreover, variations in the volume of PAN deposited on the silicon wafer may further impact the mechanical properties observed. Despite these nuances, the data underscores the power of AFM in detecting surface-level mechanical shifts that reflect broader structural phenomena. Despite these factors, the AFM-based indentation study confirms that PAN nanofibers with higher surface area achieve greater covalent bonding with ABS upon heat treatment. This suggests their potential for designing mechanically robust co-continuous interphase layers at CF-matrix interfaces. Before going to experiments with CF-reinforced composites, our goal is to establish a digital framework to predict the interfacial properties of these CF-reinforced composites nano-engineered with PAN nanofibers for their efficient design, focusing on nanofiber architecture (diameter, surface area, chain alignment, among others) and their peripheral covalent bonding effects with ABS on the interfacial interactions between carbon fibers and the matrix materials. Our previous work demonstrated that incorporating just 0.01 *wt*.% PAN nanofibers into ABS led to a remarkable ~ 20% increase in tensile strength and a ~ 60% enhancement in elastic modulus, driven by nanoscale reinforcement and interfacial interactions [29]. Our future research will systematically investigate the impact of varying PAN nanofiber content on the mechanical performance of ABS composites, aiming to optimize their structural integrity and functionality.

Computational modeling for predicting interfacial properties of nano-engineered composites

We employed all-atomic MD simulations to assess the interfacial strength of PAN nanofiber-reinforced CF-ABS composites. Given the experimentally synthesized PAN nanofiber diameters ranging from 200 to 500 nm, constructing an all-atom model for such large diameters is computationally infeasible. Consequently, we modeled smaller PAN nanofibers with diameters of 60 Å, 80 Å, and 100 Å. First, 216 PAN chains, each composed of 150 repeating units of CH_2=CHCN, were modeled and assembled into fibers

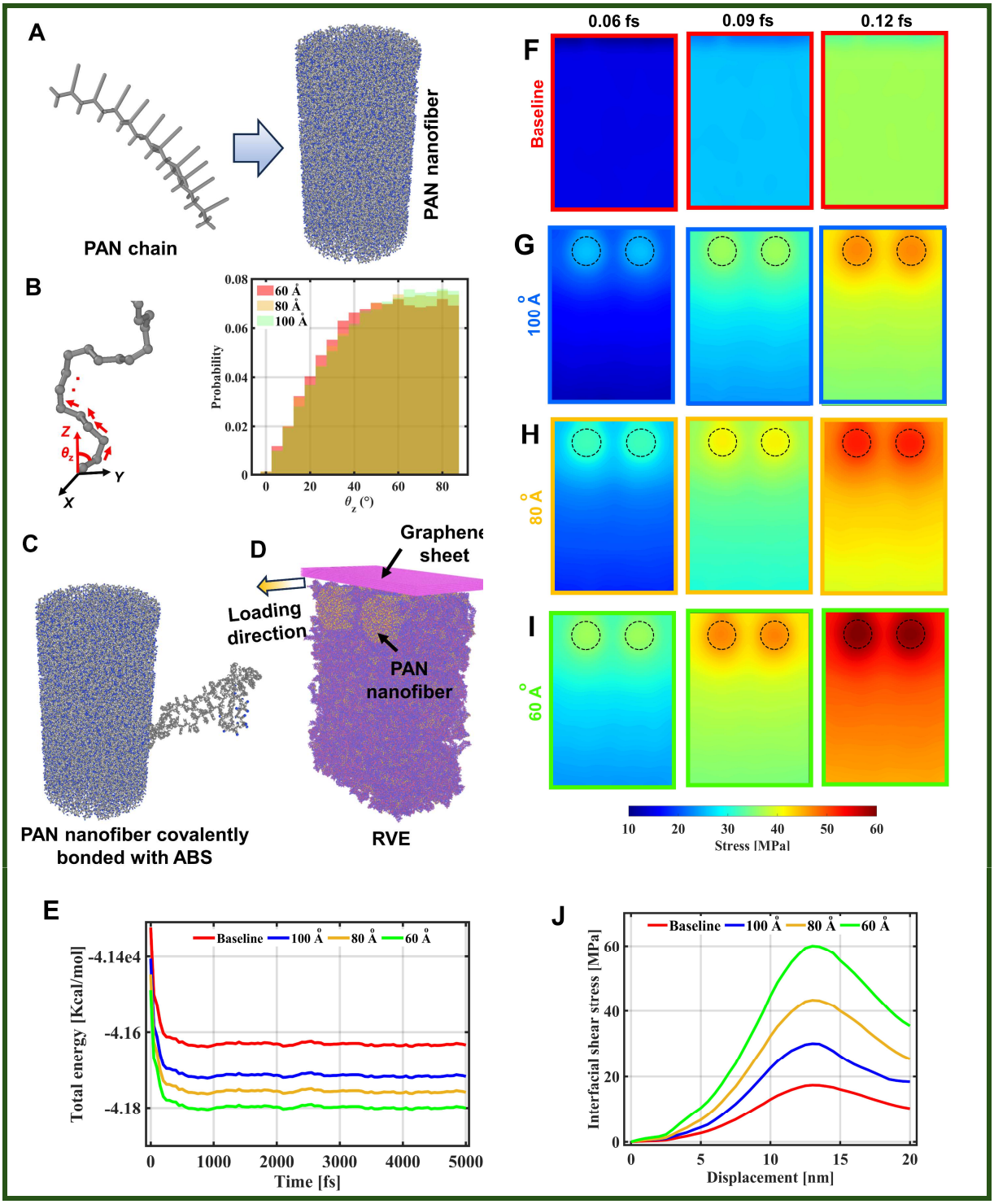

Fig. 6. MD simulations were conducted to computationally assess the mechanical performance of the nano-engineered composites. (A) PAN chains were assembled into nanofibers of various diameters, and **(B)** the orientation of individual PAN chains relative to the highlighted axis was determined. **(C)** PAN chains on the nanofiber surfaces were covalently bonded with ABS chains, then **(D)** incorporated into the ABS matrix and positioned over a graphene sheet for MD simulation. (**E**) Highlights the total energy of the composite system during equilibrium. The graphene sheet was pulled out, and the resulting stress contours are shown for (**F**) the baseline, (**G**) 100 Å, (**H**) 80 Å, and (**I**) 60 Å diameter nanofiber-containing composite RVEs. (**J**) Displays the displacement vs. interfacial shear stress plots for the composites.

of varying diameters (**Fig. 6A)**. The surface area and length of the fibers varied with diameter, directly influencing the number of nitrile groups available for potential covalent bonding with ABS chains as outlined in **Table S2**. The computational details of nanofiber modeling are included in the supporting information. Our findings indicate that smaller-diameter PAN nanofibers have higher counts of surface nitrile groups, which are critical for covalent bonding with ABS. The $PAN_{60\ Å}$ nanofibers presented 312 surface nitrogen atoms, while the $PAN_{100\ Å}$ nanofibers had only 121. Although the exact numbers may vary due to the random packing of PAN chains, the trend supports our hypothesis that smaller-diameter fibers offer more reactive sites for covalent bonding with the matrix molecules. To establish a reasonable computational framework, we assumed that ~ $1/6^{th}$ of these nitrile groups would form covalent bonding with ABS. This assumption allowed for efficient simulation of covalent bonding while highlighting the role of nanofiber surface area in determining composites' performance. Our computational analysis reveals that as the diameter of PAN nanofibers decreases, the alignment of individual PAN chains along the nanofiber axis (Z direction) significantly improves. Specifically, in 60 Å diameter nanofibers, the backbone chains of PAN molecules exhibit a notably reduced probability of orientation perpendicular to the Z axis (Fig. 6B). Additionally, the probability of PAN chains orienting perpendicular to the X and Y axes is marginally higher in 60 Å fibers compared to larger diameters (**Fig. S8**). These results clearly indicate that smaller-diameter nanofibers facilitate superior axial alignment of PAN chains, validating their enhanced structural organization. These computational results are consistent with our WAXS findings (**Fig. 3C**), which also showed improved chain alignment in the axial direction for smaller diameter PAN nanofibers. This alignment suggests that smaller diameter nanofibers should exhibit superior mechanical properties along their axial direction. Detailed methods for calculating the orientation of PAN chains with respect to fixed axes could be found in Chahal *et al* [43].

The modeled nanofibers were covalently bonded circumferentially to the ABS molecules, as schematically shown in **Fig. 6C**. As mentioned earlier, the number of covalently bonded PAN-ABS molecules at the nanofiber surfaces was systematically varied across nanofibers of different diameters. The representative template illustrating the covalently bonded PAN-ABS molecules is provided in **Fig. 4C**. Since chemical reactions do not occur between PAN and carbon fibers, their interaction is governed primarily by van der Waals forces, which were rigorously analyzed through this computational study. In short, the crosslinked PAN nanofibers were embedded within the ABS matrix and compacted to achieve the desired density to obtain PAN nanofiber-ABS unit cells. Detailed modeling procedures are provided in supporting information. The PAN-ABS unit cells were then placed in close proximity to the graphene sheets, and the system was allowed to relax prior to the *in silico* pull-out test. Three graphene sheets were utilized as analogues for the CFs due to the significantly larger diameter of CFs compared to the dimensions of the polymer molecules. This approximation allows for the assumption of an infinite radius for the CFs in comparison to the polymer molecules [44]. Following equilibration, *in silico* pull-out simulations were conducted, involving the controlled displacement (along the nanofiber axis, **Fig. 6D**) of graphene sheets from the PAN-ABS unit cell. A pull-out velocity of 0.5 Å/fs was applied, slightly higher than the 0.2 Å/fs used in previous studies, to optimize computational efficiency [45]. This literature supports this approach, noting that moderate velocities can effectively capture key mechanical behaviors without compromising data integrity. The total energy evolution during relaxation for systems with different PAN nanofiber diameters and varying degrees of crosslinking is shown in **Fig. 6E**. Notably, $PAN_{60\ Å}$ system exhibited the lowest potential energy (~ -4.18×10^4 Kcal/mol), with energy gradually increasing as the nanofiber diameter increased. For instance, the potential energy $PAN_{80\ Å}$ and $PAN_{100\ Å}$ systems rose to -4.175×10^4 Kcal/mol and -4.171×10^4 Kcal/mol, respectively. Lower potential energy indicates a more stable state, suggesting enhanced interfacial interaction between the nanofibers and the polymer matrix. This result supports our hypothesis that systems with the smallest PAN nanofibers underwent maximum PAN-ABS covalent bonding, achieve the lowest potential energy and, consequently, the highest stability.

The displacement of the graphene sheet and the deformation within the polymer representative volume element (RVE) at different time steps are shown in **Fig. S9. Figs. 6F-6I** illustrate the stress distribution

within the RVEs containing PAN nanofibers with diameters of 60 Å, 80 Å, and 100 Å, respectively, at different simulation times (0.06, 0.09, and 0.12 fs). The color contours represent the Cauchy stress, derived from MD-estimated virial stresses (**Fig. S10**), with the calculation procedures detailed in the supporting information. As the simulation progresses, increasing stress is observed within the RVEs, particularly concentrated around the PAN nanofiber locations. Notably, the induced stress within the composites increases as the diameter of the PAN nanofibers decreases. Composites containing 60 Å diameter PAN nanofibers exhibit the highest stress, reaching ~ 60 MPa, whereas those with 100 Å diameter nanofibers show a lower induced stress of ~ 50 MPa. Overall, these stress contours highlight the enhanced capacity of smaller-diameter PAN nanofibers to sustain higher stress levels under the same applied displacement at the fiber-matrix interfaces, emphasizing their superior load-bearing capability. This effectiveness is attributed to the synergistic effects of PAN chain alignment within the nanofibers and extensive peripheral crosslinking with adjacent ABS chains. Stronger PAN nanofibers (*i.e.*, smaller diameter), with their intra- and inter-chain crosslinking, create a more continuous pathway for load transfer from the matrix to the fibers.

Fig. 6J presents the interfacial smoothed shear stress versus pull-out displacement, with raw data available in **Fig. S11.** The pull-out stress initially rises with increasing displacement, followed by a drop, consistent with the behavior expected as van der Waals forces resist the initial motion of the graphene sheet. The $PAN_{60Å}$ specimens exhibit the highest interfacial strength of ~ 60 MPa, decreasing to ~ 43 MPa and ~ 30 MPa for the $PAN_{80\ Å}$ and $PAN_{100\ Å}$ composites, respectively. While a direct comparison with experimental results is limited by the smaller diameter of PAN nanofibers used in the simulations, the results indicate that incorporating finer PAN nanofibers with increased surface area and extensive covalent bonding with the ABS at the CF-matrix interfaces can substantially enhance the interfacial strength of composites. An additional contributing factor could be the strengthened π-π stacking interactions between the PAN-ABS bonded structures and adjacent graphene sheets, leading to improved interfacial properties. This model serves as a digital platform to guide interface design in composite materials by optimizing PAN nanofiber diameter, surface area, and circumferential crosslinking with the ABS matrix.

Our findings reveal that smaller-diameter PAN nanofibers exhibit enhanced molecular chain alignment along their axial direction, resulting in nanofibers with higher stiffness. Additionally, smaller-diameter nanofibers present a greater surface area and a higher number of exposed nitrile groups on their outer surfaces compared to larger-diameter nanofibers. These factors collectively minimize the stiffness mismatch between the carbon fiber and the polymer matrix, effectively forming a co-continuous interphase with intermediate stiffness at the fiber-matrix interface. This optimized interphase facilitates more efficient load transfer from the fiber to the matrix. Moreover, PAN nanofibers with a higher density of covalent bonds to ABS chains exhibit lower interfacial energy, indicating enhanced stability through stronger van der Waals interactions, thereby significantly improving the interfacial properties of the fiber-reinforced polymer composites. Table S2 presents a summary of the key findings from our computational study, highlighting the correlation between nanofiber diameter, surface area, chain alignment, and resulting interfacial strength. The results clearly demonstrate that smaller-diameter PAN nanofibers exhibit a higher surface area and provide more surface-exposed nitrile groups for reactions with adjacent ABS chains. Additionally, these nanofibers show improved PAN chain alignment along the nanofiber axis, further contributing in enhancing the composites' interfacial performance.

Composites' mechanical property testing

Finally, we conducted mechanical tests on PAN nanofiber-enhanced CF-reinforced ABS composites. Before casting these composites, it is crucial to understand how PAN nanofiber introduction influences the fiber-matrix interfacial behavior at the single fiber level. The single fiber pull-out test, widely used to assess IFSS in fiber-reinforced composites, involves embedding a single fiber within a polymer matrix before

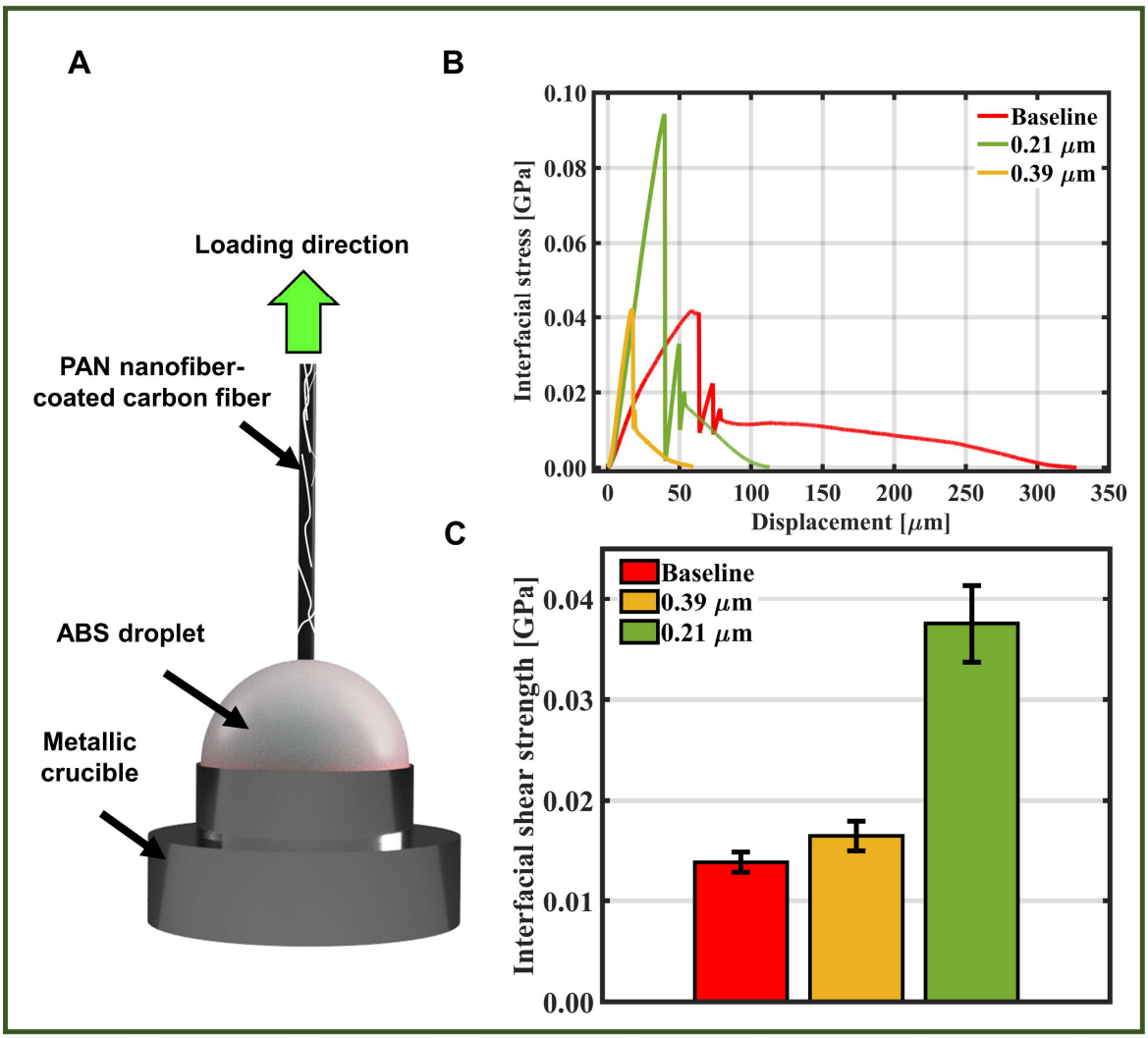

Fig. 7. A single fiber pull-out test was conducted to assess the interfacial strength of composites enhanced with PAN nanofibers of varying diameters. (B) Displays representative interfacial stress-displacement plots for these composites. **(C)** Summarizes the interfacial shear strength of the composites. Error bars denote the standard deviation from three tested single fiber specimens per set.

curing. After insertion, the polymer is cured, and an axial pull-out force is applied to the free end of the fiber to pull it out from the matrix. More detail about the theory of single fiber pull-out could be found elsewhere [46]. Single fiber pull-out specimen is schematically shown in **Fig. 7A**. Detailed sample preparation procedures are described in the experimental section. **Fig. 7B** displays typical load vs. displacement curves for single fiber specimens with different PAN nanofiber diameters. $PAN_{0.21\mu m}$ specimen exhibit the highest stiffness compared to $PAN_{0.39\mu m}$ and baseline specimens. The baseline has an IFSS of 0.027 GPa, which increases to 0.033 GPa for $PAN_{0.39\mu m}$ specimens. Notably, $PAN_{0.21\mu m}$ specimens show a dramatic improvement, with an IFSS of 0.075 GPa, ~ 250% higher than the pristine CF baseline (**Fig. 7C**). This suggests that smaller diameter PAN nanofibers, with their higher surface area, offer more reactive nitrile groups that form covalent bonds with the adjacent ABS matrix, creating co-continuous interphases between CF and the ABS polymer matrix, thus enhancing IFSS. This result aligns with the trend predicted by our computational study.

Having confirmed that smaller-diameter PAN nanofibers enhance the interfacial strength of CF-ABS composites at the single-fiber level, subsequent experiments focused on evaluating these improvements in bulk composites. Detailed sample preparation steps are outlined in the experimental procedure section and schematically shown in **Fig. S12** and **S13**. To assess the maximum influence of PAN nanofiber diameter on the mechanical properties of the FRPCs, we deposited nanofibers aligned in the loading direction. Such geometrical alignment of these nanofibers in the loading direction maximizes mechanical properties, as found in our study included in **Fig. S14**. Stress-strain plots for all composites with different diameter PAN nanofibers are shown in **Fig. 8A**, and their tensile strengths are summarized in **Fig. 8B**. $PAN_{0.21\ \mu m}$ composites exhibited the highest tensile strength of 64 MPa, ~ 56% higher than the pristine CF-ABS baseline. Tensile strength decreased with increasing nanofiber diameter, approaching the strength of pristine CF-ABS composites. A similar trend was observed for E where $PAN_{0.21\ \mu m}$ composites had an $E \approx$ 2 GPa, compared to 1.6 GPa for pristine CF. For $PAN_{0.39\ \mu m}$ composites, E dropped to ~ 1.5 GPa (**Fig. 8C**). Fracture energy also followed this trend, with $PAN_{0.21\ \mu m}$ composites showing the highest fracture energy of 133 N-mm, ~175% higher than the pristine CF composite (**Fig. 8D**). Larger fibers, with less tensile strength and surface area, resulted in lower number of covalent bonding with ABS, leading to less pronounced mechanical properties similar to the pristine CF composite. Insufficiently bonded larger nanofibers, characterized by lower mechanical properties due to reduced alignment of PAN chains, may act as local defects, thereby deteriorating the overall mechanical performance of the composites. Overall, the mechanical test results presented in **Figs. 8A-8D** validate our computational hypothesis that increased PAN-ABS covalent bonding with the higher surface area of the PAN nanofibers, combined with axially aligned PAN chains enhances interfacial strength of the composites by promoting stronger non-bonded van der Waals interactions between the crosslinked nanofibers and carbon fibers.

For further validation, we performed fractography on the fractured composite surfaces, examining them with SEM. In pristine CF composites (**Fig. 8E**), we observed bare CF surfaces, indicating weak fiber-matrix interaction. On the contrary, as the PAN nanofiber diameter decreased, the amount of residual ABS polymer on the CF surfaces increased (**Figs. 8F-8H**). This suggests stronger fiber-matrix interaction with smaller-diameter PAN nanofibers. The scaffold network of electrospun PAN nanofibers at the fiber-matrix interface remains intact and distinctly visible in $PAN_{0.21\mu m}$ composites, owing to their superior mechanical properties resulting from PAN chain alignment (**Fig. 8H**). Our computational study corroborates these findings, demonstrating that smaller-diameter PAN nanofibers possess higher counts of surface nitrile groups, which promote covalent bonding with the ABS matrix. This leads to the formation of an interconnected co-continuous network with improved affinity towards CF, thereby enhancing the overall performance of the composite.

We also studied the stiffness components of the composites using low-field NMR relaxometry distinguishing between rigid, intermediate, and mobile phase fractions [47]. In rigid phases, where molecular motion is restricted, relaxation times are shorter due to strong dipole-dipole interactions. In contrast, mobile phases exhibit longer relaxation times because of increased molecular mobility and reduced dipole-dipole interactions. Intermediate phases show relaxation times that lie between these two extremes. By analyzing the distribution of relaxation times, we quantified the relative proportions of rigid, intermediate, and mobile phases within a composite. In our case, it can be assumed that the total rigid volume arises from the CFs and the nanofiber-enhanced PAN-ABS components, while the intermediate fraction is solely derived from the interphase volume (*i.e.*, PAN-ABS crosslinked structure), and the mobile fraction originates from the ABS matrix, as schematically shown in **Fig. 8I**. It is shown that the rigid fraction of the $PAN_{0.21\mu m}$ composites is ~ 10% higher, with an intermediate component volume increase of ~ 5 % (**Fig. 8J**) and a mobile fraction reduction of 5% (**Fig. 8K**) compared to the pristine CF composite. This trend is logical, as PAN nanofibers become covalently bonded with the ABS matrix upon heat treatment, resulting in more immobile rigid and intermediate components within the composites. The extent of crosslinking decreases with increasing PAN nanofiber diameter due to the reduced surface area and fewer

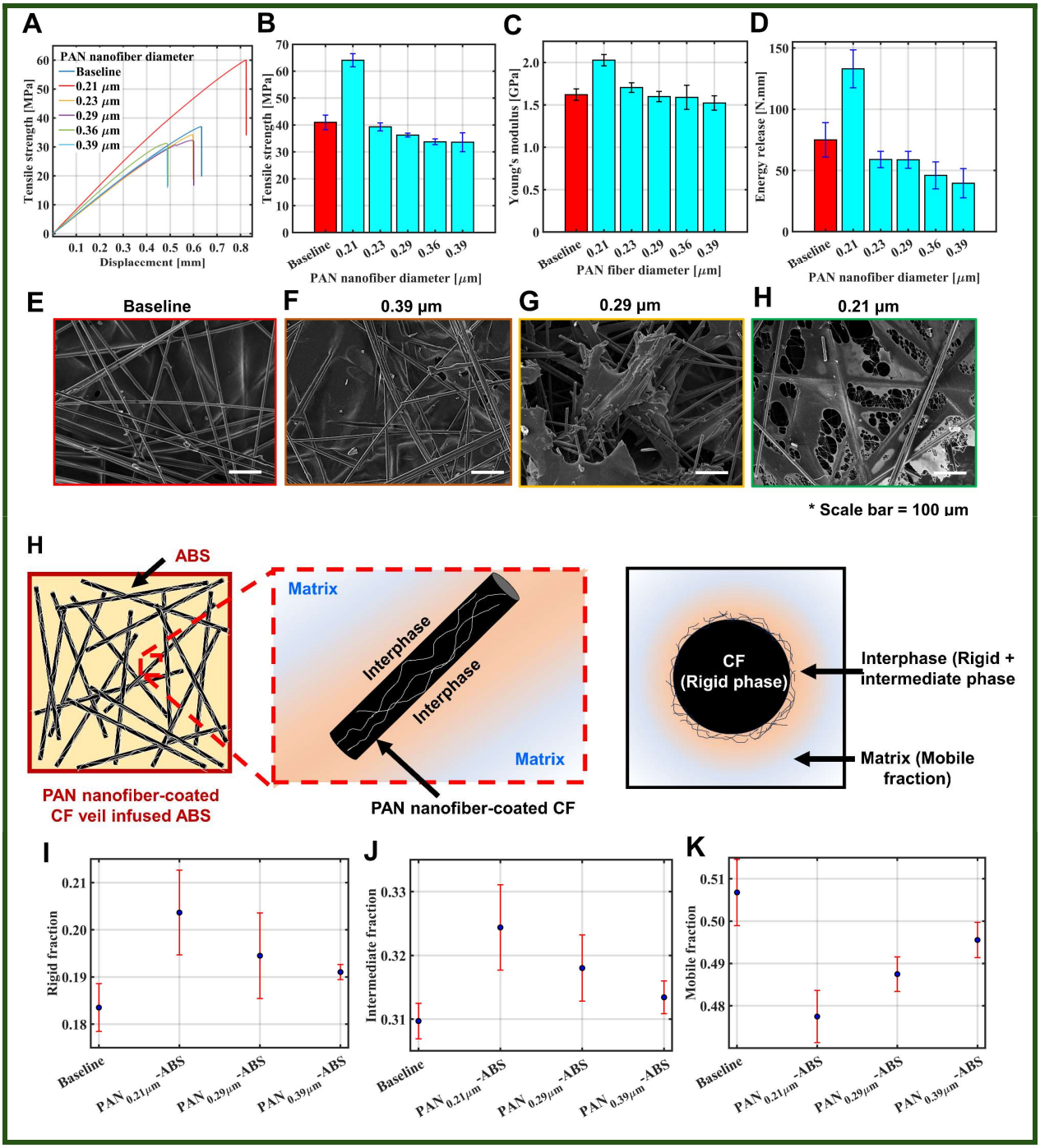

Fig. 8. PAN nanofibers were integrated at the carbon fiber-matrix interfaces, and the interfacial properties of the bulk composites were systematically analyzed. **(A)** Representative stress-strain curves for composites with varying diameters of PAN nanofibers. Summary of (**B**) tensile strength, (**C**) *E*, (**D**) energy release during fracture. Error bars represent the standard deviation from six composite specimens. (**E**), (**F**), (**G**), and (**H**) SEM images of fractured composite surfaces for pristine CF and composites with PAN nanofibers of 0.39, 0.29, and 0.21 μm diameters, respectively. **(I)** provides a schematic representation of the three stiffness components in composites, as analyzed by solid-state NMR relaxometry. **(J)**, **(K)**, and **(L)** are the rigid, intermediate, and mobile fractions of the composites with different diameter PAN nanofibers obtained from low-field NMR relaxometry study. Error bars indicate the standard deviation from three composite specimens.

active nitrile groups available for covalent bonding with the ABS matrix. Furthermore, reduced alignment of PAN chains within individual larger nanofibers lowers their stiffness, diminishing their contribution to the composite's rigid and intermediate stiffness components. Collectively, these findings validate our hypothesis that the physicochemical reinforcing effect of PAN nanofibers, attributed to their higher surface area and superior molecular alignment, can be strategically exploited to enhance composite interface strength by integrating them at the carbon fiber-matrix interface and covalently tethering them to the matrix.

Conclusions

The fiber-matrix interphase remains the most vulnerable region in FRPCs due to the inherent disparity in stiffness between the fibers and the polymer matrix, which hampers effective load transfer. Over the past decades, numerous attempts have been made to nanoengineer the fiber-matrix interface using various polymers and nanomaterials. While these efforts have yielded positive results, they often face challenges related to scalability and high costs. In this paper, we present a novel methodology that addresses these challenges by leveraging a physicochemical reinforcing mechanism of chemically active nanofibers integrated at the fiber-matrix interfaces. By meticulously controlling the surface area and molecular chain alignment of these nanofibers and ensuring the presence of compatible functional groups, we enable covalent bonding with the matrix molecules. This approach creates a multiscale bridge between the fibers and the matrix, forming a co-continuous network that facilitates efficient load transfer between the fibers and the matrix. Unlike other methods, our technique offers the potential to overcome the limitations of intensive chemical processing, scalability, and associated costs. We demonstrate the feasibility of this approach using a composite system comprising chopped CFs and ABS as the matrix, with electrospun PAN as the nanofibers. The architecture of PAN nanofibers, including surface area and molecular chain alignment, was precisely controlled by varying electrospinning parameters. The compatible nitrile groups in PAN and ABS enable covalent bonding between the nanofibers and the matrix upon suitable heat treatment. To the best of our knowledge, this is the first report of an interphase design process that leverages physiochemical reinforcing effect of a chemically transformable thermoplastic nanofibers by optimizing nanofiber architecture and leveraging their covalent bonding with the adjacent matrix. The scientific understanding developed here can be readily extended to other polymeric composite systems, potentially enhancing their strength-to-weight ratios and advancing the field of FRPCs.

In this study, we successfully fabricated electrospun PAN nanofibers by varying the V and the r, achieving significant control over nanofiber diameter, surface area, molecular chains, and nanofiber alignments. Increasing r to 2,500 rpm enhanced the nanofiber alignment by 50%, as quantified by the HOF. Simultaneously, adjusting V influenced the PAN nanofiber diameter, with lower V yielding smaller diameters and greater surface areas, thereby improving PAN chain alignment. Heat treatment at 250˚C for 30 minutes facilitated effective covalent bonding between the PAN nanofibers and ABS, resulting in more interconnected structures within the composite matrix. Comprehensive analyses, including solubility tests, rheology, TGA, and DSC, revealed that composites with smaller-diameter PAN nanofibers exhibited superior chemical integrity, enhanced viscoelastic properties, and improved thermal stability. AFM-based nanoindentation confirmed that these composites contained regions of higher mechanical stiffness. Computational modeling supported our findings, demonstrating that covalently bonded PAN-ABS nanofibers have enhanced interfacial properties compared to their pristine counterparts, and possess a stronger affinity towards CFs. Consequently, FRPCs with these nanofibers showed remarkable improvements in mechanical performance: a 56% increase in tensile strength, a 25% increase in E, and a dramatic 175% increase in fracture energy release. Low-field solid-state NMR relaxometry further revealed that composites with smaller-diameter PAN nanofibers had increased rigid and intermediate volume fractions indicating increased interphase region formation contributing to their superior mechanical properties.

While our proof-of-concept was demonstrated using a simple CF-based PAN-ABS composite system, the scientific insights gained suggest that this approach could be broadly applicable to the composites where

nanofibers and matrix materials possess compatible chemical groups capable of covalent interaction under suitable external stimuli. The principles established here have significant potential to inform the design of tougher composites across various industries, including additive manufacturing, aerospace, and automotive sectors, where high specific strength is critically important. For instance, based on our developed platform and modeling, ABS composites enhanced with ultra-low concentrations of PAN and subjected to heat treatment during 3D printing could yield significantly tougher 3D-printed structures. Overall, our method offers a promising solution to the longstanding challenge of weak interphases in composite materials. By forming a robust, scalable, co-continuous interphases at the fiber-matrix interface, this approach has the potential to break through the traditional barriers in composite manufacturing, paving the way for the development of tougher, more durable composites.

Experimental details

The materials for this research were obtained from different suppliers: chopped CF veil from Composite Envisions, LLC, and GP35 ABS pellets from M-Holland, LLC. The PAN powder used is composed of copolymers with 95.36 mol.% acrylonitrile and 4.64 mol.% methyl acrylate, having a molecular weight of 126 kDa and a polydispersity index of 2.23. Acetone, dimethylformamide (DMF), chloroform ($CHCl_3$), and dimethyl sulfoxide (C_2H_6OS) were sourced from Fisher Scientific LLC.

Electrospinning: For electrospinning, a 5 *wt*.% PAN solution was prepared by dissolving approximately 0.99 g of PAN powder in 20 mL of DMF. The mixture was stirred continuously at 300 rpm for ~ 48 h using a magnetic stirrer until the PAN powder was fully dissolved, forming a clear, golden-yellowish solution. This solution was then transferred into a syringe fitted with a blunt-tip needle for the electrospinning process. The resulting PAN nanofibers were deposited onto two substrates - aluminum foil and CF veils before being used in various experiments.

Substrates measuring 457 × 152 mm² were secured around a grounded cylindrical collector, which was rotated at various *r*. The electrospinning process was conducted using different *V*, with the needle tip positioned ~ 14 cm from the collecting drum. A syringe pump rate of 0.75 mL/h was maintained for all the electrospinning. A schematic of the fabrication setup is shown in **Fig. S1**.

To prepare samples for morphological analysis via SEM, a 10-nm-thick layer of gold particles was sputter-coated onto the ~ 30 s electrospun PAN-coated aluminum foil. SEM imaging was performed using a TESCAN MIRA3 microscope, operating at an accelerating voltage of 10 kV.

To investigate the orientation of PAN molecules, WAXS experiments were performed using a Xeuss 3.0 SAXS/WAXS instrument (Xenocs, France) equipped with a Dectris Eiger 2R 4M hybrid photon counting detector, featuring a pixel dimension of 75 × 75 μm. PAN specimens for WAXS were prepared by continuously depositing approximately 20 mL of PAN solution onto aluminum foil, which were then isolated and suspended over a sample holder. During electrospinning, a rotation speed of 2,500 rpm was maintained to align most nanofibers along the drum's rotation direction. The D2+ MetalJet X-ray source (GaKα, λ = 1.341 Å) was used as the incident beam, with a 3-minute exposure time. The sample-to-detector distance was set at 55 mm, and all scattering data were collected under vacuum in transmission mode.

Specimen Preparation: PAN-ABS composites with ~ 0.02 *wt*.% PAN fibers were prepared by shear-mixing electrospun PAN nanofibers with ABS pellets at 150°C. The total shear-mixing time was limited to 30 min with a mixing speed of 60 rpm. ABS pellets were added into the mixer and shear mixing was performed for 12 min followed by addition PAN fibers and mixed for an additional 18 min. PAN fibers deposited on aluminum foil with different *V*s and at 2,500 rpm were used in this step. Total 20 mL of PAN-DMF dope was electrospun at a time to prepare PAN nanofiber films which were also used in WAXS and DSC experiments. The shear-mixed PAN-ABS beads were hot-pressed (~ 958 kPa, ~ 30 min) at 250˚C. The hot-pressed PAN-ABS plates were cut into small pieces and used in solubility tests. These small pieces

were also used in DSC and TGA study. From $(PAN\text{-}ABS)_{250°C}$ plate, 10-mm-diameter, 1-mm-thick circular discs were cut out for the rheology test.

For the AFM study, we prepared PAN-ABS films by depositing PAN nanofibers on a silicon wafer for ~ 30 seconds, followed by spin-coating (2,000 rpm for ~ 1 min) with 10 *wt*.% ABS-acetone emulsion (**Fig. 6A**). The films were dried at room temperature for ~ 24 h, heat-treated at 250°C for ~ 30 minutes, and tested using a Cypher AFM.

We prepared single fiber samples by isolating a single CF from the tow and coating it with different diameter PAN nanofibers via electrospinning. A grounded metallic surface was placed directly behind the CF to create a uniformly distributed electric field, preventing excessive accumulation of PAN nanofibers on the CF surface. The PAN nanofiber-coated carbon fiber was then carefully inserted into a 10 *wt*.% ABS-acetone emulsion drop-casted into a metallic crucible (**Fig. 7A**) using the Textechno FIMABOND embedding station. After ~ 24 h of curing at room temperature, the specimens were subjected to 250˚C heat treatment for ~ 30 min followed by testing in the Textechno FAVIMAT+ single fiber pull-out test setup.

Composite laminates were prepared by stacking eight CF veils, each face coated with electrospun PAN nanofibers via ~ 30 s of electrospinning. These sheets were then dip-coated in a 10 *wt*.% ABS emulsion in acetone (**Fig. S12**) and allowed to dry at room temperature for ~ 24 h. The ABS-acetone emulsion was prepared by dissolving about 52.3 g of ABS pellets in 600 mL of acetone, mixed at 500 rpm for ~ 24 h at room temperature. Eight ABS-coated CF veils were subsequently hot-pressed at 250°C under constant pressure of approximately 958 kPa for ~ 30 minutes (**Fig. S13**). The resulting FRPC panels were then precision-cut into 100 × 10 mm² rectangular specimens using a water jet cutter. These pieces were tabbed with 25 × 10 mm² Garolite strips in preparation for in-plane shear strength testing (**Fig. S13**).

The tested composite specimens were cut into small pieces and divided into three sets to perform the low-field NMR-based relaxometry.

Testing Protocols: The gel content was determined using a solvent extraction method. Both neat ABS and heat-treated PAN-ABS composites, with varying PAN nanofiber diameters, were analyzed. Each sample was initially weighed (M_i) before being immersed in a 15 mL solvent mixture of DMSO and $CHCl_3$ (1:1, w/w) for 48 hours in a 20 mL glass vial at 60°C. After extraction, the specimens were dried in a vacuum oven at 120°C for 24 hours and then reweighed (M_d). The gel fraction was calculated according to Equation 1.

$$\text{Gel fraction} = \frac{M_d}{M_i} \times 100 \tag{1}$$

Rheological measurements were conducted using a DHR-3 rotational rheometer (TA Instruments, New Castle, DE) equipped with 8 mm stainless steel parallel plates, operating in an air atmosphere. To prevent any slippage of the composites during testing, the rheometer was set to apply a constant compressive force of 1 N. The system was then cooled to 150°C and held for approximately one minute before initiating the test. An oscillatory frequency sweep was subsequently carried out with a shear strain of 0.1%, allowing for the analysis of the dynamic response of the PAN-ABS composite over an angular frequency range from 0.01 to 100 rad/s. The shear strain value was selected based on the linear viscoelastic region identified from a prior amplitude-frequency sweep study.

DSC experiments were conducted using a DSC Q2000, in a nitrogen atmosphere, ranging from -10°C to 310°C, with a heating rate of 10°C/min. All the tests were performed in a nitrogen environment to ensure consistency. Similarly, TGA was performed using a TGA Q500 with similar temperature ramp experiments conducted in an air atmosphere.

The nanomechanical mapping presented in **Fig. 5** was carried out in air using a Cypher AFM system from Asylum Research. The tips used were PPP-NCLPt with a nominal spring constant of ≈ 48N/m. The nanomechanical measurements were performed using the AM-FM mode, consisting of exciting the cantilever at its 1st and 2nd bending eigenmodes, respectively, and using the 1st in Amplitude modulation mode (AM) to track the topography and the 2nd in Frequency modulation (FM) to track the indentation, from which local stiffness can be determined, using the Hertz model. The 1st mode was excited at ≈159kHz and the 2nd mode was excited at ≈987kHz.

IFSS in single fiber pullout study was determined from the observed peak load (F_{max}) using the formula in **Equation 2**

$$IFSS = \frac{F_{\max}}{\pi D L_e} \tag{2}$$

where D is the average diameter of fiber (~ 5 μm) and L_e is the fiber embedment length which is also determined from the pull-out load-displacement curves.

Mechanical testing was conducted using a displacement-controlled Instron tensile load frame equipped with a 10 kN load cell. The tests were performed under tension at a displacement rate of 1 mm/min until the composite specimens failed. Load versus crosshead displacement data were recorded at a frequency of 10 Hz. For each set of composites, the average width and thickness of five specimens were measured to assess tensile and in-plane shear strength. Each set comprised a total of six specimens.

To probe the combination of rigid, intermediate, and mobile fractions in the PAN-ABS samples, low-field ^{1}H NMR measurements were performed using a Minispec MQ20. For low-field NMR testing, composite samples were cut into small squares of approximately 3x3 mm. A single 3 μs 90° pulse with a 10 μs dead time was applied, and the decay signal was collected up to approximately 300 μs. The collected free induction decay (FID) signal was modeled using a three-component fit, comprising Gaussian, Weibullian, and mono-exponential functions to represent the behavior of rigid (A_G), intermediate (A_{Wb}), and mobile (A_{exp}) protons, respectively (eq. X) [48]. Phase fractions of each sample were compared to elucidate how the morphology of electrospun PAN influences the phase distribution in the PAN-ABS-CF composites.

$$A(t) = A_G\left\{\exp\left[-\left(\frac{t}{T_{2G}}\right)^2\right]\right\} + A_{Wb}\left\{\exp\left[-\left(\frac{t}{T_{2Wb}}\right)^{1.5}\right]\right\} + A_{exp}\left\{\exp\left[-\left(\frac{t}{T_{2exp}}\right)\right]\right\} \tag{3}$$

Acknowledgements

This manuscript had been authored by UT-Battelle, LLC under Contract No. DE-AC05-00OR22725 with the U.S. Department of Energy. The United States Government retains and the publisher, by accepting the article for publication, acknowledges that the United States Government retains a non-exclusive, paid-up, irrevocable, worldwide license to publish or reproduce the published form of this manuscript or allow others to do so, for United States Government purposes. The Department of Energy will provide public access to these results of federally sponsored research in accordance with the DOE Public Access Plan (http://energy.gov/downloads/ doe-public-access-plan). This research at Oak Ridge National Laboratory, managed by UT Battelle, LLC, for the U.S. Department of Energy (DOE) under Contract No. DE-AC05-00OR22725, was sponsored by the Vehicle Technologies Office (VTO) (Award #: DE-LC-0000021) within the Office of Energy Efficiency and Renewable Energy (EERE). LTK and MT acknowledge support from the US Department of Energy, Office of Science, Basic Energy Sciences, Materials Sciences, and Engineering Division [FWP#ERKCK60] for X-ray and NMR characterization of nanofiber-matrix interface. AFM imaging was performed (MC, LC, II) at the Center for Nanophase Materials Sciences (CNMS), which is a US Department of Energy, Office of Science User Facility at ORNL. This research used resources of the Oak Ridge Leadership Computing Facility at the Oak Ridge National Laboratory,

which is supported by the Office of Science of the U.S. Department of Energy under Contract No. DE-AC05-00OR22725.

References

[1] H. Ku, H. Wang, N. Pattarachaiyakoop, and M. Trada, "A review on the tensile properties of natural fiber reinforced polymer composites," *Composites Part B: Engineering,* vol. 42, no. 4, pp. 856-873, 2011.

[2] H. Li *et al.*, "A review of carbon fiber surface modification methods for tailor-made bond behavior with cementitious matrices," *Progress in Materials Science,* vol. 132, no. 101040, 2023.

[3] I. C. Finegan, G. G. Tibbetts, D. G. Glasgow, J. M. Ting, and M. L. Lake, "Surface treatments for improving the mechanical properties of carbon nanofiber/thermoplastic composites," *Journal of Materials Science,* vol. 38, pp. 3485-3490, 2003.

[4] J. Jiang, X. Yao, C. Xu, Y. Su, L. Zhou, and C. Deng, "Influence of electrochemical oxidation of carbon fiber on the mechanical properties of carbon fiber/graphene oxide/epoxy composites," *Composites Part A: Applied Science and Manufacturing,* vol. 95, pp. 248-256, 2017.

[5] J. Yu, L. Meng, D. Fan, C. Zhang, F. Yu, and Y. Huang, "The oxidation of carbon fibers through K2S2O8/AgNO3 system that preserves fiber tensile strength," *Composites Part B: Engineering,* vol. 60, pp. 264-267, 2014.

[6] H. Zhang and W. Li, "Plasma-grafting polymerization on carbon fibers and its effect on their composite properties," *Applied Surface Science,* vol. 356, pp. 492-498, 2015.

[7] F. Liu, Z. Shi, and Y. Dong, "Improved wettability and interfacial adhesion in carbon fibre/epoxy composites via an aqueous epoxy sizing agent," *Composites Part A: Applied Science and Manufacturing,* vol. 112, pp. 337-345, 2018.

[8] Y. Ma, T. Yokozeki, M. Ueda, T. Sugahara, Y. Yang, and H. Hamada, "Effect of polyurethane dispersion as surface treatment for carbon fabrics on mechanical properties of carbon/Nylon composites," *Composites Science and Technology,* vol. 151, pp. 268-281, 2017.

[9] S. Chen, Y. Cao, and J. Feng, "Polydopamine as an efficient and robust platform to functionalize carbon fiber for high-performance polymer composites," *ACS Applied Materials & Interfaces,* vol. 6, no. 1, pp. 349-356, 2014.

[10] X. Yang, H. Du, S. Li, Z. Wang, and L. Shao, "Codepositing mussel-inspired nanohybrids onto one-dimensional fibers under “green” conditions for significantly enhanced surface/interfacial properties," *ACS Sustainable Chemistry & Engineering,* vol. 6, no. 3, pp. 4412-20, 2018.

[11] W. Han, H. P. Zhang, J. Tavakoli, J. Campbell, and Y. Tang, "Polydopamine as sizing on carbon fiber surfaces for enhancement of epoxy laminated composites," *Composites Part A: Applied Science and Manufacturing,* vol. 107, pp. 626-632, 2018.

[12] M. D. Batista and L. T. Drzal, "Carbon fiber/epoxy matrix composite interphases modified with cellulose nanocrystals," *Composites Science and Technology,* vol. 164, pp. 274-281, 2018.

[13] Q. Wu, R. Zhao, Q. Liu, T. Jiao, J. Zhu, and F. Wang, "Simultaneous improvement of interfacial strength and toughness between carbon fiber and epoxy by introducing amino functionalized ZrO2 on fiber surface," *Materials & Design,* vol. 149, pp. 15-24, 2018.

[14] X. Zhang *et al.*, "Interfacial microstructure and properties of carbon fiber composites modified with graphene oxide," *ACS Applied Materials & Interfaces,* vol. 4, no. 3, pp. 1543-1552, 2012.

[15] L. Ma *et al.*, "Reinforcing carbon fiber epoxy composites with triazine derivatives functionalized graphene oxide modified sizing agent," *Composites Part B: Engineering,* vol. 176, p. 107078, 2019.

[16] S. Gupta, A. K. Naskar, and C. C. Bowland, "An engineered multifunctional composite for passive sensing, power harvesting, and in situ damage identification with enhanced mechanical performance," *Advanced Materials Technologies,* vol. 7, no. 9, p. 2101549, 2022.

[17] S. M. Rankin, M. K. Moody, A. K. Naskar, and C. C. Bowland, "Enhancing functionalities in carbon fiber composites by titanium dioxide nanoparticles," *Composites Science and Technology,* vol. 201, p. 108491, 2021.

[18] M. Felisberto *et al.*, "Carbon nanotubes grown on carbon fiber yarns by a low temperature CVD method: A significant enhancement of the interfacial adhesion between carbon fiber/epoxy matrix hierarchical composites. ," *Composites Communications,* vol. 3, pp. 33-37, 2017.

[19] P. Lv, Y. Y. Feng, P. Zhang, H. M. Chen, N. Zhao, and W. Feng, "Increasing the interfacial strength in carbon fiber/epoxy composites by controlling the orientation and length of carbon nanotubes grown on the fibers," *Carbon,* vol. 49, no. 14, pp. 4665-73, 2011.

[20] X. Chen, H. Xu, D. Liu, C. Yan, and Y. Zhu, "A facile one-pot fabrication of polyphosphazene microsphere/carbon fiber hybrid reinforcement and its effect on the interfacial adhesion of epoxy composites," *Applied Surface Science,* vol. 410, pp. 530-539, 2017.

[21] L. Shi *et al.*, "The effect of self-synthesized hydroxyl-terminated hyperbranched polymer interface layer on the properties of carbon fiber reinforced epoxy composites," *Applied Surface Science,* vol. 479, pp. 334-343, 2019.

[22] G. Wang *et al.*, "Improving the interfacial and flexural properties of carbon fiber–epoxy composites via the grafting of a hyperbranched aromatic polyamide onto a carbon fiber surface on the basis of solution polymerization," *Journal of Applied Polymer Science,* vol. 136, no. 12, p. 47232, 2019.

[23] Q. Wu *et al.*, "Enhanced mechanical properties of multiscale carbon fiber/epoxy composites by fiber surface treatment with graphene oxide/polyhedral oligomeric silsesquioxane," *Advanced Materials Interfaces,* vol. 6, no. 21, p. 1900970, 2019.
[24] K. Peng, A. Nain, and R. Mirzaeifar, "Tracking the origins of size dependency in the mechanical properties of polymeric nanofibers at the atomistic scale," *Polymer,* vol. 175, pp. 118-128, 2019.
[25] K. Peng and R. Mirzaeifar, "Interplay of chain orientation and bond length in size dependency of mechanical properties in polystyrene nanofibers," *ACS Applied Polymer Materials,* vol. 2, no. 4, pp. 1664-1671, 2020.
[26] S. Buell, G. C. Rutledge, and K. J. Vliet, "Predicting polymer nanofiber interactions via molecular simulations," *ACS Applied Materials & Interfaces,* vol. 2, no. 4, pp. 1164-1172, 2010.
[27] M. Naraghi, S. N. Arshad, and I. Chasiotis, "Molecular orientation and mechanical property size effects in electrospun polyacrylonitrile nanofibers," *Polymer,* vol. 52, no. 7, pp. 1612-1618, 2011.
[28] R. Palazzetti and A. J. Zucchelli, "Electrospun nanofibers as reinforcement for composite laminates materials–a review," *Composite Structures,* vol. 182, pp. 711-727, 2017.
[29] S. Gupta *et al.*, "Enhancing composite toughness through hierarchical interphase formation," *Advanced Science,* vol. 11, no. 6, p. 2305642, 2024.
[30] S. Huan *et al.*, "Effect of experimental parameters on morphological, mechanical and hydrophobic properties of electrospun polystyrene fibers," *Materials,* vol. 8, no. 5, pp. 2718-34, 2015.
[31] I. Lasenko, D. Grauda, D. Butkauskas, J. V. Sanchaniya, A. Viluma-Gudmona, and V. Lusis, "Testing the physical and mechanical properties of polyacrylonitrile nanofibers reinforced with succinite and silicon dioxide nanoparticles," *Textiles,* vol. 2, no. 1, pp. 162-73, 2022.
[32] M. Naraghi and S. N. A. I. Chasiotis, "Molecular orientation and mechanical property size effects in electrospun polyacrylonitrile nanofibers," *Polymer,* vol. 52, no. 7, pp. 1612-8, 2011.
[33] M. Xu, D. N. Futaba, T. Yamada, M. Yumura, and K. Hata, "Carbon nanotubes with temperature-invariant viscoelasticity from–196 to 1000 C," *Science,* vol. 330, no. 6009, pp. 1364-8, 2010.
[34] H. Tang, M. H. Malakooti, and H. A. Sodano, "Relationship between orientation factor of lead zirconate titanate nanowires and dielectric permittivity of nanocomposites," *Applied Physics Letters,* vol. 103, no. 22, 2013.
[35] A. Baji, Y. W. Mai, S. C. Wong, M. Abtahi, and P. Chen, "Electrospinning of polymer nanofibers: Effects on oriented morphology, structures and tensile properties," *Composites Science and Technology,* vol. 70, no. 5, pp. 703-718, 2010.
[36] J. M. Deitzel, J. Kleinmeyer, D. E. Harris, and N. B. Tan, "The effect of processing variables on the morphology of electrospun nanofibers and textiles," *Polymer,* vol. 42, no. 1, pp. 261-72, 2001.
[37] K. P. Matabola and R. M. Moutloali, "The influence of electrospinning parameters on the morphology and diameter of poly (vinyledene fluoride) nanofibers-effect of sodium chloride," *Journal of Materials Science,* vol. 48, pp. 5475-82, 2013.
[38] N. Grassie and R. McGuchan, "Pyrolysis of polyacrylonitrile and related polymers - Thermal analysis of polyacrylonitrile," *European Polymer Journal,* vol. 6, no. 9, pp. 1277-91, 1970.
[39] X. Hou, X. Yang, L. Zhang, E. Waclawik, and S. Wu, "Stretching-induced crystallinity and orientation to improve the mechanical properties of electrospun PAN nanocomposites," *Materials & Design,* vol. 31, no. 4, pp. 1726-30, 2010.
[40] B. Szepcsik and B. Pukánszky, "The mechanism of thermal stabilization of polyacrylonitrile," *Thermochimica Acta,* vol. 671, pp. 200-208, 2019.
[41] S. J. Buwalda, K. W. Boere, P. J. Dijkstra, J. Feijen, T. Vermonden, and W. E. Hennink, "Hydrogels in a historical perspective: From simple networks to smart materials," *Journal of Controlled Release,* vol. 190, pp. 254-73, 2014.
[42] "AM-FM Viscoelastic Mapping Mode," in *Asylum Research*, ed. Santa Barbara, CA: Oxford Instruments, 2014.
[43] R. Chahal *et al.*, "Deep-learning interatomic potential connects molecular structural ordering to the macroscale properties of polyacrylonitrile," *ACS Applied Materials & Interfaces,* vol. 16, no. 28, pp. 36878-91, 2024.
[44] Y. Yan *et al.*, "Molecular dynamics simulation of the interface properties of continuous carbon fiber/polyimide composites," *Applied Surface Science,* vol. 563, p. 150370, 2021.
[45] L. Yang, L. Tong, and X. He, "MD simulation of carbon nanotube pullout behavior and its use in determining mode I delamination toughness," *Computational Materials Science,* vol. 55, pp. 356-364, 2012.
[46] A. Pearson, W. Liao, Y. Kazemi, A. Kakroodi, A. Hammami, and H. Naguib, "Interfacial shear strength of glass fiber reinforced polyketone measured by the single fiber pullout test," in *AIP Conference Proceedings 2023*, 2023, vol. 2607: AIP Publishing.
[47] J. P. Patel and S. L. Hsu, "Development of low field NMR technique for analyzing segmental mobility of crosslinked polymers," *Journal of Polymer Science Part B: Polymer Physics,* vol. 56, no. 8, pp. 639-643, 2018.
[48] V. Räntzsch *et al.*, "Polymer crystallinity and crystallization kinetics via benchtop 1H NMR relaxometry: revisited method, data analysis, and experiments on common polymers," *Polymer,* vol. 145, pp. 162-173, 2018.